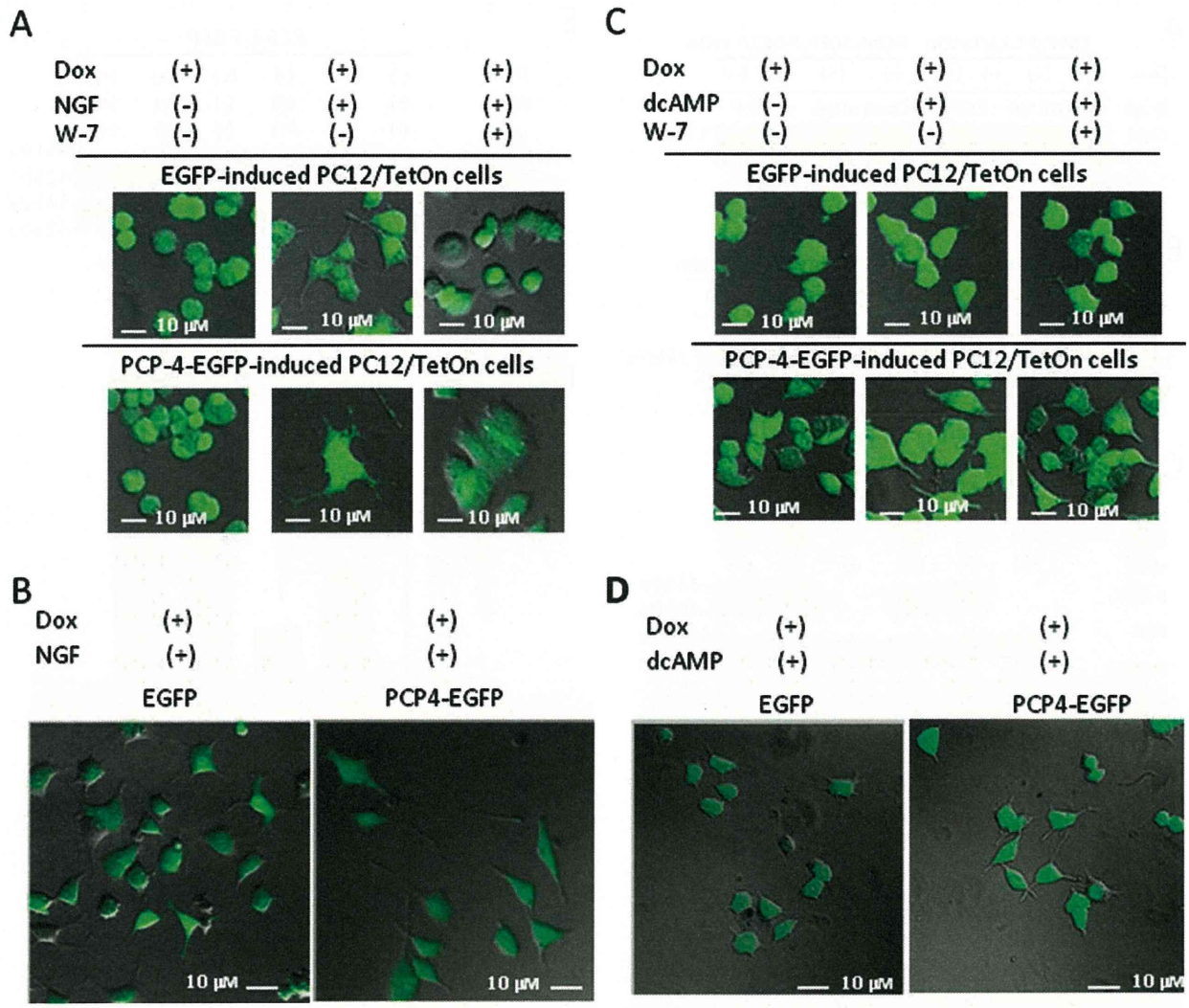

Fig. 3. PCP4 advances neurite outgrowth and increases size of cell body. **A,B:** Neurite outgrowth and size of cell body detected by fluorescent micrographs after treatment with 50 ng/ml NGF ± 50 μM W-7 for 48 hr in EGFP-induced (A, upper panel; B, left panel) or PCP4-EGFP-induced PC12/TetOn cells (A, lower panel; B, right panel). **C,D:** Neurite outgrowth and size of cell body detected by fluorescent micrographs after treatment with 0.5 mM dcAMP ± 50 μM W-7 for 12 hr in EGFP-induced (C, upper panel; D, left panel) or in PCP4-EGFP-induced PC12/TetOn cells (C, lower panel; D, right panel). **E–J:** Quantification of neurite outgrowth and size of cell body treated with 50 ng/ml NGF or 0.5 mM dcAMP in EGFP- or PCP4-EGFP-induced PC12/TetOn cells. Time course of average length of neurite outgrowth treated with 50 ng/ml NGF for 4 days (E) or with 0.5 mM dcAMP for 24 hr (F) quantified by neurite outgrowth quantification assay. Average neurite outgrowth treated with 50 ng/ml NGF for 4 days (G) or with 0.5 mM dcAMP for 24 hr (H) measured by confocal microscopy using NIH Image (n = 50). Average area of the cells treated with 50 ng/ml NGF for 4 days (I) or with 0.5 mM dcAMP for 24 hr (J) analyzed by confocal microscopy using NIH Image (n = 50). **K,L:** Effect of PD98059, an ERK inhibitor, on ERK phosphorylation and neurite outgrowth in PCP4-EGFP-induced PC12/TetOn cells. Western blot analysis shows that ERK phosphorylation induced by 50 ng/ml NGF is completely blocked by 50 μM PD98059 (K). Fluorescent micrographs (n = 50; upper panel) and neurite quantification assay (lower panel) show inhibition of neurite outgrowth in the presence of 50 μM PD98059 and 50 ng/ml NGF for 48 hr (L). **M:** Effect of PMA on neurite outgrowth in PCP4-EGFP-induced PC12/TetOn cells. Fluorescent micrographs (n = 50) (upper panel) and neurite quantification assay (lower panel) show neurite outgrowth in the presence of 50 ng/ml NGF and 100 nM PMA with or without PKC inhibitor for 48 hr. Images are representative of three independent experiments. Data are means ± SE of three independent experiments. $*P < 0.05$, $**P < 0.01$. Dox, doxycycline; NGF, nerve growth factor; PKCI, PKC inhibitor.

that in EGFP-induced PC12/TetOn cells, which was partially inhibited by 50 μM W-7 (Fig. 3A,B). In a similar fashion, with 0.5 mM dcAMP treatment for 12 hr, neurite outgrowth was moderately increased in PCP4-EGFP-induced PC12/TetOn cells compared with that in EGFP-induced PC12/TetOn cells, and 50 μM W-7 partially inhibited neurite outgrowth (Fig. 3C,D). Neurite outgrowth quantification assay and measurement of

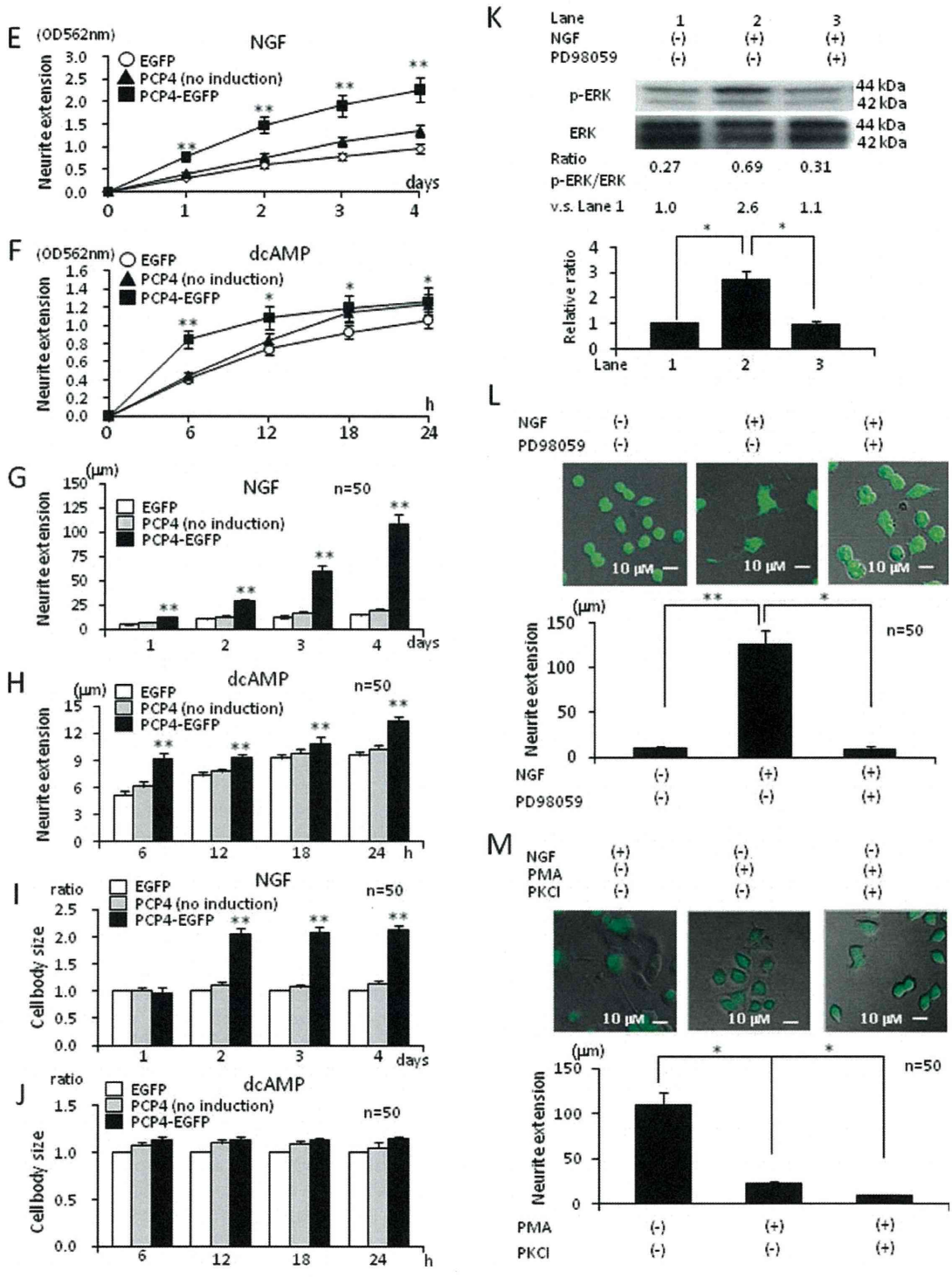

Fig. 3. (Continued)

neurite length by confocal microscopy also showed much greater neurite extension in PCP4-EGFP-induced PC12/TetOn cells than in EGFP-induced PC12/TetOn cells in the presence of 50 ng/ml NGF (Fig. 3E,F). Neurite outgrowth quantification assay and confocal microscopic analysis also showed significantly more rapid

neurite extension in PCP4-EGFP-induced PC12/TetOn cells in the presence of dcAMP (Fig. 3G, H). Furthermore, fluorescent micrographs revealed that size of cell body was increased about twofold in PCP4-EGFP-induced PC12/TetOn cells by treatment with NGF (Fig. 3A,B,I); size of cell body was not increased by the treatment with dcAMP (Fig. 3C,D,J). We then wanted to determine whether PD98059, an ERK inhibitor, inhibits PCP4-enhanced neurite outgrowth. After induction of PCP4-EGFP with 1 μg/ml dox for 48 hr, the culture media were changed, and PCP4-EGFP-induced PC12/TetOn cells were incubated with 50 μM PD98059 for 30 min in the presence of 1 μg/ml dox, followed by 48 hr of additional culture with 50 ng/ml NGF. PD98059 almost completely blocked ERK phosphorylation (Fig. 3K) and neurite outgrowth (Fig. 3L), indicating that ERK is important for PCP4-mediated cell signaling in PC12 cells. Because PCP4 is a substrate for PKC phosphorylation (Dickerson et al., 2006), we examined the effect of PMA on neurite outgrowth. PCP4-EGFP-induced PC12/TetOn cells were incubated with 10 nM to 1 μM PMA with or without 5 μM PKC inhibitor for up to 72 hr. However, no apparent neurite outgrowth was observed in PMA-treated-PCP4-EGFP-induced PC12/TetOn cells compared with that in NGF-treated cells (Fig. 3M).

PCP4 Enhances Acetylcholine and Dopamine Release

As PC12 cells release several neurotransmitters during differentiation (Shafer and Atchison, 1991), we examined the effect of PCP4 on acetylcholine (ACh) and dopamine (DA) release. When incubated with low (4.7 mM)- or high (25 mM)-potassium buffer, both constitutive and evoked ACh release were increased about twofold in PCP4-EGFP-induced PC12/TetOn cells compared with that in EGFP-induced PC12/TetOn cells (Fig. 4A). Constitutive and potassium-evoked DA release also were increased by about twofold (see Fig. 5B), and DA uptake was slightly but significantly increased in PCP4-EGFP-induced PC12/TetOn cells (Fig. 4C). On the other hand, 50 μM W-7 inhibited such PCP4-enhanced ACh and DA release and DA uptake (Fig. 4A–C).

PCP4 Inhibits H_2O_2-Induced Apoptosis

We examined the inhibitory effect of PCP4 on H_2O_2-induced apoptosis in PC12/TetOn cells. After treatment with dox for 48 hr, EGFP- or PCP4-EGFP-induced PC12/TetOn cells were incubated with H_2O_2 for 24 hr. H_2O_2-induced apoptosis defined by DNA fragmentation was observed at 0.2 and 1.0 mM H_2O_2 in EGFP-induced PC12/TetOn cells (Fig. 4D). On the other hand, H_2O_2-induced apoptosis was inhibited in PCP4-EGFP-induced PC12/TetOn cells (Fig. 4D). Caspase-3 activity also was increased in H_2O_2-treated EGFP-induced PC12/TetOn cells, but it was decreased by about 60% in H_2O_2-treated PCP4-EGFP-induced PC12/TetOn cells (Fig. 4E). Furthermore, ananxin-V-positive and BOBO-1-negative apoptotic cells detected on fluorescent micrographs were increased in H_2O_2-treated control PC12 cells. However, such apoptotic cells were decreased to about one-third in PCP4-EGFP-induced PC12/TetOn cells compared with that in control or PCP4-EGFP-uninduced PC12/TetOn cells (Fig. 4F).

Knockdown of PCP4 Decreases Neurite Outgrowth and Dopamine Release and Increases Apoptosis

PCP4 expression in PC12 cells was then knocked down. PCP4 endogenously expressed in PC12 cells and two types of PCP4 siRNAs or scramble siRNAs were transfected into PC12 cells. Number 2 PCP4 siRNAs effectively knocked PCP4 expression down to about 7% compared with number 2 scramble siRNA (Fig. 5A). Therefore, we selected number 2 scramble siRNA and number 2 PCP4 siRNA for the following experiments. PC12 cells were transfected with scramble siRNA or PCP4 siRNAs, cultured for 48 hr, and then incubated with 50 ng/ml NGF for an additional 48 hr. Neurite outgrowth was decreased to about 30% in PCP4 siRNA-transfected PC12 cells compared with that in scramble siRNA-transfected PC12 cells (Fig. 5B). High potassium (25 mM)-evoked dopamine release was decreased by about 35% in PCP4 siRNA-transfected PC12 cells compared with that in scramble siRNA-transfected PC12 cells (upper panel), although the difference in dopamine uptake was not significantly altered between the two cells (lower panel; Fig. 5C). H_2O_2-induced caspase-3 activity (upper panel) and apoptotic cells positive for annexin-V and negative for BOBO-1 (lower panel) were also increased at 24 hr in PCP4 siRNA-transfected PC12 cells compared with scramble siRNA-transfected PC12 cells (Fig. 5D).

DISCUSSION

Our present study shows that PCP4 advances neurite outgrowth in the presence of NGF, increases ACh and DA release, and inhibits H_2O_2-induced apoptosis. These phenomena all are produced through regulation of calcium-binding calmodulin function.

Calmodulin is a key molecule for transmitting calcium signaling in cells and has multiple functions (Bähler and Rhoads, 2002; Xia and Storm, 2005). The molecule is regulated by small calmodulin binding proteins that have an IQ motif (Slemmon et al., 2000; Bähler and Rhoads, 2002). Representative molecules are neuromodulin, neurogranin, and PCP4. All of these bind calcium-poor calmodulin and modify calmodulin functions. Phosphorylation of neurogranin and neuromodulin by PKC allows calmodulin to be released by an increase in intracellular calcium, by which signaling is transmitted in cells (Slemmon et al., 2000; Gaertner et al., 2004). PCP4 also is phosphorylated by PKC (Dickerson, et al., 2006). Phosphorylated PCP at serine resides might bind

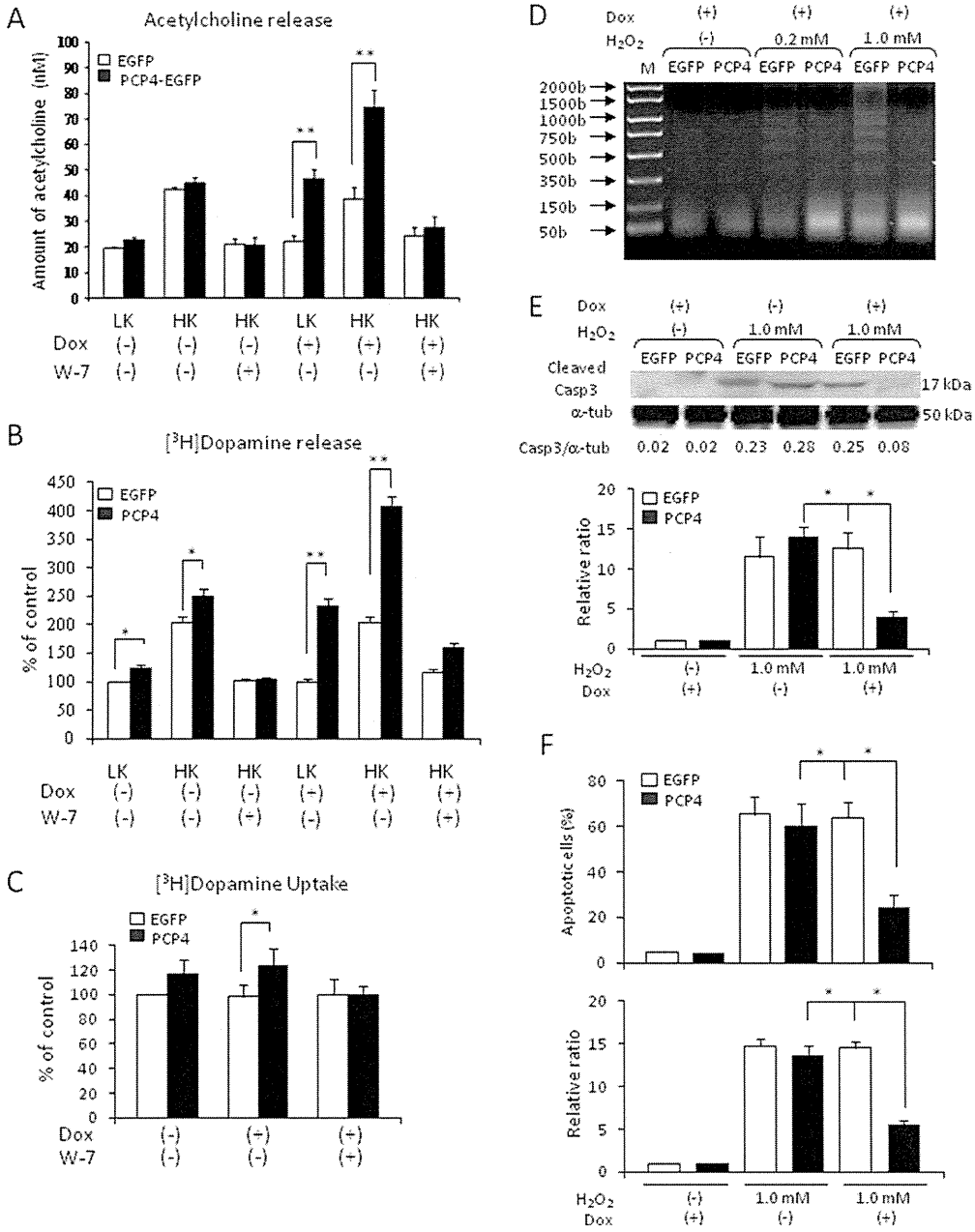

Fig. 4. PCP4 increases acetylcholine and dopamine release and inhibits apoptosis induced by H_2O_2 in PC12/TetOn cells. **A:** Measurement of acetylcholine release after treatment with low (4.7 mM)- or high (25 mM)-potassium conditions ± 50 μM W-7 for 10 min in EGFP- or PCP4-EGFP-induced PC12/TetOn cells. **B:** Measurement of dopamine release after treatment with low (4.7 mM)- or high (25 mM)-potassium conditions ± 50 μM W-7 for 6 min in EGFP- or PCP4-EGFP-induced PC12/TetOn cells. **C:** Dopamine uptake incubated with [^{3}H]dopamine for 10 min in the presence or absence of 50 μM W-7 in EGFP- or PCP4-EGFP-induced PC12/TetOn cells. **D:** Detection of DNA fragmentation after incubation with 0.2 mM or 1.0 mM H_2O_2 for 24 hr in EGFP- or PCP4-EGFP-induced PC12/TetOn cells. **E:** Western blot analysis of caspase-3 activity induced by 1.0 mM H_2O_2 for 24 hr in EGFP- or PCP4-EGFP-induced PC12/TetOn cells. **F:** Relative ratio of annexin-V-postive and BOBO-1-negative apoptotic cells detected by fluorescent micrographs in the absence or presence of 1.0 mM H_2O_2 for 24 hr in EGFP- or PCP4-EGFP-induced PC12/TetOn cells. Images are representative of three independent experiments. Data are means ± SE of three independent experiments. $*P < 0.05$, $**P < 0.01$. Dox, doxycycline; Casp3, caspase-3; α-tub, α-tubulin; LK, low potassium (4.7 mM); HK, high potassium (25 mM).

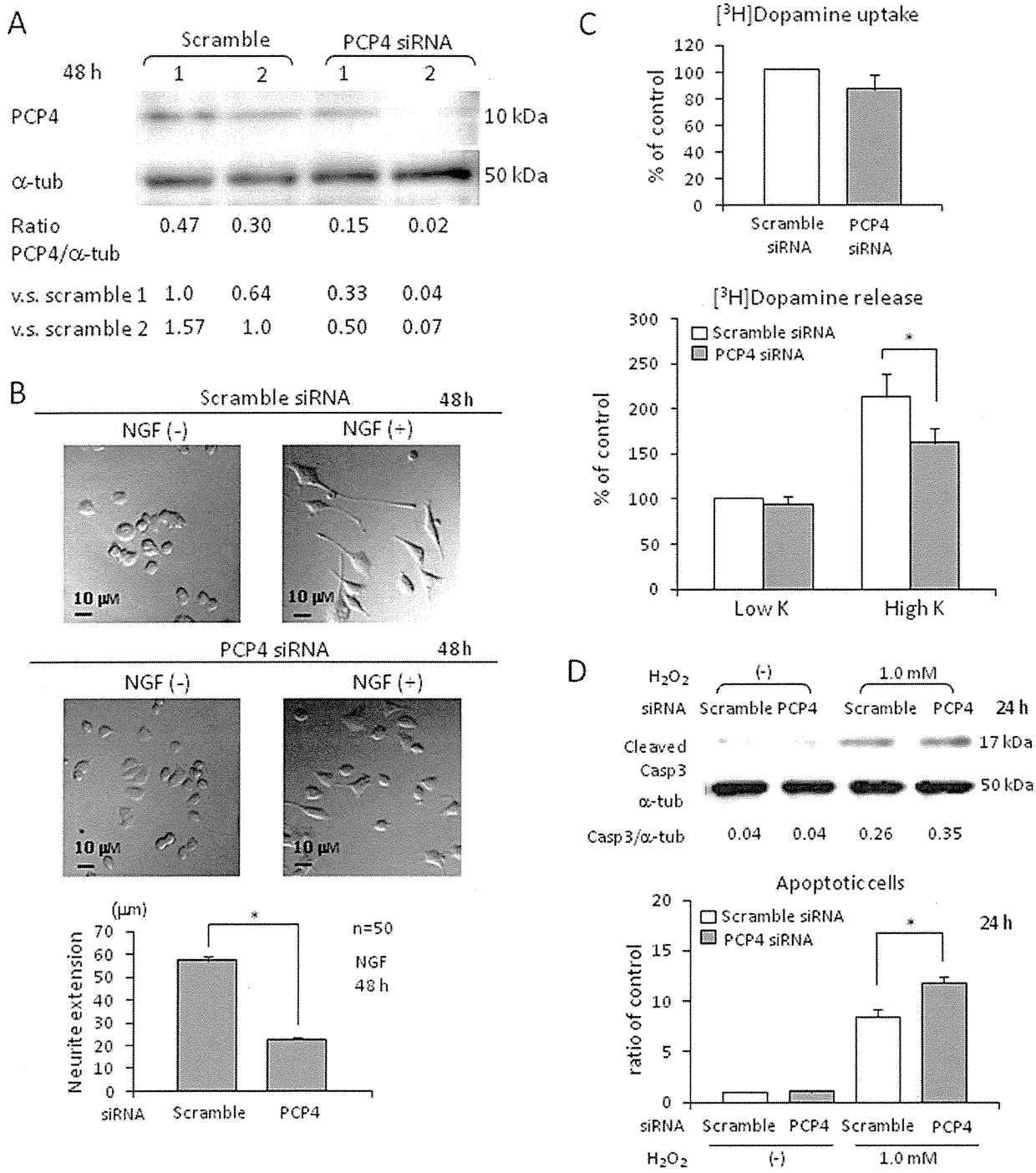

Fig. 5. Knockdown of PCP4 decreases neurite outgrowth, dopamine release, and antiapoptotic effect. **A:** PCP4 expression detected by Western blot analysis in siRNA-transfected PC12 cells (48 hr). **B:** Brightfield micrographs of scramble (upper panel) or PCP4 (middle panel) siRNA-transfected PC12 cells and neurite outgrowth quantified by confocal microscopy using NIH Image (n = 50; lower pannel) in scramble or PCP4 siRNA-transfected PC12 cells in the presence or absence of 50 ng/ml NGF (48 hr). **C:** Dopamine uptake and potassium-evoked dopamine release from scramble or PCP4 siRNA-transfected PC12 cells. **D:** H_2O_2-induced apoptosis. Caspase-3 activity was detected by Western blot analysis (24 hr; upper panel), and annexin-V-positive and BOBO-1-negative apoptotic cells were detected by fluorescent micrographs (24 hr; lower panel) in scramble or PCP4 siRNA-transfected PC12 cells. Images are representative of three independent experiments. Data are means ± SE of three independent experiments. $*P < 0.05$. Dox, doxycycline; Casp3, caspase-3; α-tub, α-tubulin; LK, low potassium (4.7 mM); HK, high potassium (25 mM).

to both calcium-binding calmoduin and calcium-free calmodulin (Dickerson et al., 2006), and the rate of PCP4 binding to calcium-free calmodulin is at least 50-fold less than that to calcium-binding calmodulin (Kleerekoper and Putkey, 2009). PCP4 regulates calmodulin-mediated signaling pathways by accelerating the rates of association and dissociation of calcium from the C-domain of calmodulin as well as that of calmodulin binding to other proteins (Putkey et al., 2003). Neurogranin and neuromodulin are thought to regulate negatively calcium-binding calmodulin function by binding calcium-free calmodulin; PCP4 may positively modulate calcium-binding calmodulin activity. Indeed, CaMKII is fully activated in PCP4-overexpressing PC12 cells when calcium influx is achieved with ATP (Johanson et al., 2000). Apoptosis induced by UV or staurosporine is inhibited by overexpression of PCP4 in PC12 cells (Erhardt et al., 2000). On the other hand, neurogranin amplifies susceptibility to NO-induced apoptosis (Gui et al., 2007).

Our results also suggest that PCP4 activates calmodulin-mediated functions. Induction of PCP4 inhibits H_2O_2-induced apoptosis in PC12/TetOn cells through activation of calmodulin function. The calmodulin/CaMKII/GSK-3 pathway has an important role in antiapoptosis in PC12 cells (Takadera and Ohyashiki, 2007) and neurons (Song et al., 2010). We therefore speculate that the antiapoptotic effect of PCP4 also is mediated by the calmodulinin/CaMKII pathway. In addition, ACh and DA release are augmented and neurite outogrowth is advanced in the presence of NGF and dcAMP in PCP4-EGFP-induced PC12/TetOn cells. Importantly, PCP4 enhanced the effect of NGF in PC12 cells. Neurite outgrowth and size of cell body were much greater by treatment with NGF than those by dcAMP. NGF and calmodulin are key elements in the modulation of Ras and MAP kinase signaling (Agell et al., 2002). In fact, the process of neurite extension was accompanied by changes in the morphology of the cells such as increase in cell body size (Bar-Sagi and Feramisco, 1985). Increased size of cell body suggests active protein synthesis, followed by initiation of neurite outgrowth and increase in ACh and DA release. However, degeneration of neurites was found not to affect size of cell body (Bar-Sagi and Feramisco, 1985). In the present study, although W-7 inhibited neurite extension and ACh and DA release, it did not completely decrease size of cell body, indicating that calmodulin/Ras signaling is important for neurite outgrowth and neurotransmitter releases, whereas another signal such as PI3 kinase or mTOR, which is not directly downstream of the PCP4/calmodulin signal, also is involved in protein synthesis. On the other hand, dcAMP was found to advance neurite outgrowth independently of the Ras signal (Agnel et al., 2002), and the neurites of the dcAMP-treated PCP4-induced PC12 cells were finer than those of the NGF-treated PCP4-induced PC12 cells, as previously observed (Bar-Sagi and Feramisco, 1985), suggesting that the neurite outgrowth by dcAMP is independent of protein synthesis. Indeed, dcAMP did not affect size of cell body in PCP4-induced PC12 cells. Furthermore, activation of PKC by PMA did not affect neurite outgrowth in PCP4-induced PC12 cells, even though PCP4 phosphorylated by PKC binds to both calcium-binding and -free calmodulin. So far, it is unclear whether phosphorylation of PCP4 positively or negatively regulates calmodulin function. However, it is possible that PCP4 positively regulates calmodulin function with other stimuli such as NGF, because the serine residue in PCP4 is displaced by only one amino acid when compared with neurogranin and neuromodulin, which are negative regulators of calmodulin (Dickerson et al., 2006).

It has been shown that PCP4 does not act globally to suppress calmodulin activity but rather changes the manner in which different stimuli elicit the activity (Johanson et al., 2000). It also has been reported that reduced levels of PCP4 indicate that neurons that are less competent to regulate calmodulin-mediated intracellular pathways and more prone to neural death, insofar as expression of this molecule is about 34% decreased in Alzheimer's disease and is almost totally absent in Huntington's disease (Utal et al., 1998). Based on our results and previous reports, PCP4 may affect calmodulin function cooperatively with other stimuli in neuronal or neuroendocrine cell differentiation in a manner different that of from neuromodulin and neurogranin.

REFERENCES

Agell N, Bachs O, Rocamora N, Villalonga P. 2002. Modulation of the Ras/Raf/MEK/ERK pathway by Ca^{2+}, and calmodulin. Cell Signal 14:649–654.

Bähler M, Rhoads A. 2002. Calmodulin signaling via the IQ motif. FEBS Lett 513:107–113.

Bar-Sagi D, Feramisco JR. 1985. Microinjection of the ras oncogene protein into PC12 cells induces morphological differentiation. Cell 42:841–848.

Cabin DE, Gardiner K, Reeves RH. 1996. Molecular genetic characterization and comparative mapping of the human PCP4 gene. Somat Cell Mol Genet 22:167–175.

Cabin DE, McKee-Johnson JW, Matesic LE, Wiltshire T, Rue EE, Mjaatvedt AE, Huo YK, Korenberg JR, Reeves RH. 1998. Physical and comparative mapping of distal mouse chromosome 16.5 p5. Genome Res 89:940–950.

Chen H, Bouras C, Antonarakis SE. 1996. Cloning of the cDNA for a human homolog of the rat PEP-19 gene and mapping to chromosome 21q22.2-q22.3. Hum Genet 98:672–677.

Chen SL, Orr HT. 1990. Sequence of a murine cDNA, pcp-4, that encodes the homolog of the rat brain-specific antigen PEP-19. Nucleic Acids Res 18:1304.

Dickerson JB, Morgan MA, Mishra A, Slaughter CA, Morgan JI, Zheng J. 2006. The influence of phosphorylation on the activity and structure of the neuronal IQ motif protein, PEP-19. Brain Res 1092:16–27.

Erhardt JA, Legos JJ, Johanson RA, Slemmon JR, Wang X. 2000. Expression of PEP-19 inhibits apoptosis in PC12 cells. Neuroreport 11:3719–3723.

Gaertner TR, Putkey JA, Waxham MN. 2004. RC3/neurogranin and Ca^{2+}/calmodulin-dependent protein kinase II produce opposing effects on the affinity of calmodulin for calcium. J Biol Chem 279:39374–39382.

Gerendasy DD, Sutcliffe JG. 1997. RC/neurogranin, a postsynaptic calpacitin for setting the response threshold to calcium influxes. Mol Neurobiol 15:131–163.

Gui J, Song Y, Han NL, Sheu FS. 2007. Characterization of transcriptional regulation of neurogranin by nitric oxide and the role of neurogranin in SNP-induced cell death: implication of neurogranin in an increased neuronal susceptibility to oxidative stress. Int J Biol Sci 3:212–224.

Hubert RS, Korenberg JR. 1997. PCP4 maps between DS21S345 and P31P10SP6 on chromosome 21q22.2→q22.3. Cytogenet Cell Genet 78:44–45.

Iwamoto K, Bundo M, Yamamoto M, Ozawa H, Saito T, Kato T. 2004. Decreased expression of NEFH and PCP4/PEP19 in the prefrontal cortex of alcoholics. Neurosci Res 49:379–385.

Johanson RA, Sarau HM, Foley JJ, Slemmon JR. 2000. Calmodulin-binding peptide PEP-19 modulates activation of calmodulin kinase II in situ. J Neurosci 20:2860–2866.

Kirino T. 1982. Delayed neuronal death in the gerbil hippocampus following ischemia. Brain Res 6:57–69.

Kleerekoper QK, Putkey JA. 2009. PEP-19, an intrinsically disordered regulator of calmodulin signaling. J Biol Chem 284:7455–7464.

Mattson MP, Kater SB. 1989. Development and selective neurodegeneration in cell cultures from different hippocampal regions. Brain Res 490:110–125.

Olson LE, Roper RJ, Baxter LL, Carlson EJ, Epstein CJ, Reeves RH. 2004. Down syndrome mouse models Ts65Dn, Ts1Cje, and Ms1Cje/Ts65Dn exhibit variable severity of cerebellar phenotypes. Dev Dyn 230:581–589.

Putkey JA, Kleerekoper Q, Gaertner TR, Waxham MN. 2003. A new role for IQ motif proteins in regulating calmodulin function. J Biol Chem 278:49667–49670.

Sangameswaran L, Hempstead J, Morgan JI. 1989. Molecular cloning of a neuron-specific transcript and its regulation during normal and aberrant cerebellar development. Proc Natl Acad Sci U S A 86:5651–5655.

Shafer TJ, Atchison WD. 1991. Transmitter, ion channel and receptor properties of phenochromocytoma (PC12) cells: a model for neurotoxicological studies. Neurotoxicology 12:473–379.

Simons SB, Escobedo Y, Yasuda R, Dudek SM. 2009. Regional differences in hippocampal calcium handling provide a cellular mechanism for limiting plasticity. Proc Natl Acad Sci U S A 106:14080–14084.

Slemmon JR, Hughes CM, Campbell GA, Flood DG. 1994. Increased levels of hemoglobin-derived and other peptides in Alzheimer's disease cerebellum. J Neurosci 14:2225–2235.

Slemmon JR, Feng B, Erhardt JA. 2000. Small proteins that modulate calmodulin-dependent signal transduction: effects of PEP-19, neuromodulin, and neurogranin on enzyme activation and cellular homeostasis. Mol Neurobiol 22:99–113.

Smith DJ, Stevens ME, Sudanagunta SP, Bronson RT, Makhinson M, Watabe AM, O'Dell TJ, Fung J, Weier HU, Cheng JF, Rubin EM. 1997. Functional screening of 2 Mb of human chromosome 21q22.2 in transgenic mice implicates minibrain in learning defects associated with Down syndrome. Nat Genet 16:28–36.

Song B, Lai B, Zheng Z, Zhang Y, Luo J, Wang C, Chen Y, Woodgett JR, Li M. 2010. Inhibitory phosphorylation of GSK-3 by CaMKII couples depolarization to neuronal survival. J Biol Chem. 285:41122–41134.

Takadera T, Ohyashiki T. 2007. Calmodulin inhibitor-induced apoptosis was prevented by glycogen synthase kinase-3 inhibitors in PC12 cells. Cell Mol Neurobiol 27:783–790.

Thomas S, Thiery E, Aflalo R, Vayssettes C, Verney C, Berthuy I, Créau N. 2003. PCP4 is highly expressed in ectoderm and particularly in neuroectoderm derivatives during mouse embryogenesis. Gene Express Patterns 3:93–97.

Utal AK, Stopka AL, Roy M, Coleman PD. 1998. PEP-19 immunohistochemistry defines the basal ganglia and associated structures in the adult human brain, and is dramatically reduced in Huntington's disease. Neuroscience 86:1055–1063.

Vaudry D, Stork PJS, Lazarovici P, Eiden LE. 2002. Signaling pathways for PC12 cell differentiation: making the right connections. Science 296:1648–1649.

Xia Z, Storm DR. 2005. The role of calmodulin as a signal integrator for synaptic plasticity. Nat Rev Neurosci 6:267–276.

Ziai MR, Pan YC, Hulmes JD, Sangameswaran L, Morgan JI. 1986. Isolation, sequence, and developmental profile of a brain-specific polypeptide, PEP-19. Proc Natl Acad Sci U S A 83:8420–8423.

Ziai MR, Sangameswaran L, Hempstead JL, Danho W, Morgan JI. 1988. An immunochemical analysis of the distribution of a brain-specific polypeptide, PEP-19. J Neurochem 51:1771–1776.

Ionic mechanisms and Ca^{2+} dynamics underlying the glucose response of pancreatic β cells: a simulation study

Chae Young Cha,[1] Yasuhiko Nakamura,[2] Yukiko Himeno,[2] JianWu Wang,[3] Shinpei Fujimoto,[2] Nobuya Inagaki,[2] Yung E Earm,[4] and Akinori Noma[1]

[1]Biosimulation Project, Faculty of Bioinformatics, Ritsumeikan University, Kusatsu, Shiga 525-8577, Japan
[2]Department of Diabetes and Clinical Nutrition, Graduate School of Medicine, Kyoto University, Kyoto 606-8501, Japan
[3]School of Public Health, Central South University, Changsha 410078, China
[4]Department of Physiology, Seoul National University, Seoul 110-749, Korea

To clarify the mechanisms underlying the pancreatic β-cell response to varying glucose concentrations ([G]), electrophysiological findings were integrated into a mathematical cell model. The Ca^{2+} dynamics of the endoplasmic reticulum (ER) were also improved. The model was validated by demonstrating quiescent potential, burst–interburst electrical events accompanied by Ca^{2+} transients, and continuous firing of action potentials over [G] ranges of 0–6, 7–18, and >19 mM, respectively. These responses to glucose were completely reversible. The action potential, input impedance, and Ca^{2+} transients were in good agreement with experimental measurements. The ionic mechanisms underlying the burst–interburst rhythm were investigated by lead potential analysis, which quantified the contributions of individual current components. This analysis demonstrated that slow potential changes during the interburst period were attributable to modifications of ion channels or transporters by intracellular ions and/or metabolites to different degrees depending on [G]. The predominant role of adenosine triphosphate–sensitive K^+ current in switching on and off the repetitive firing of action potentials at 8 mM [G] was taken over at a higher [G] by Ca^{2+}- or Na^+-dependent currents, which were generated by the plasma membrane Ca^{2+} pump, Na^+/K^+ pump, Na^+/Ca^{2+} exchanger, and TRPM channel. Accumulation and release of Ca^{2+} by the ER also had a strong influence on the slow electrical rhythm. We conclude that the present mathematical model is useful for quantifying the role of individual functional components in the whole cell responses based on experimental findings.

INTRODUCTION

The pancreatic β cell has a unique function of converting variations in the extracellular glucose concentration ([G]) to electrical activity, thereby controlling the level of insulin secretion. This signal transduction is dependent on the interaction between energy metabolism and membrane excitation. Several mechanisms have been suggested underlying this bilateral coupling in pancreatic β cells. The gating of ATP-sensitive K^+ channels is regulated by fluctuations in the intracellular concentration of ATP or MgADP ([ATP] or [MgADP]), resulting in a prolongation of the duration of the burst of action potentials with increasing [G]. The activation of L-type Ca^{2+} channels by an increase of [ATP] (Smith et al., 1989), or the depression of Na^+/K^+ pump (NaK) activity up to 50% by increasing [G] (Owada et al., 1999), may also favor burst prolongation. In addition, variations in intracellular ion concentrations may have varying influences on individual channels or transporters depending on [G]. For example, it has been recently suggested that a K^+ current activated by intracellular Ca^{2+} (I_{Kslow}) may affect bursting activity (Göpel et al., 1999a; Goforth et al., 2002). Finally, the electrical activity induces a significant increase in ion fluxes across the surface membrane, which alters energy consumption via active ion transport or Ca^{2+}-mediated processes, including insulin secretion. These pathways are all linked in a complex system, and one approach to aid the quantification of the contribution to bursting activity of individual pathways is the development of a mathematical β-cell model.

Such models have been used for nearly 30 years to elucidate the principle mechanisms underlying the bursting activity in β cells. Early stage models used a formulation consisting of a minimum number of components: two or three K^+ currents, a Ca^{2+} current, and/or a leak current (Chay and Keizer, 1983; Sherman et al., 1988, 1990; Keizer and Magnus, 1989; Smolen and Keizer, 1992; Bertram et al., 1995b). These model simulations suggested consistently the critical role of a slowly changing variable in generating the burst–interburst

C.Y. Cha and Y. Nakamura contributed equally to this paper.
Correspondence to Akinori Noma: noma@sk.ritsumei.ac.jp

Abbreviations used in this paper: BK, large-conductance Ca^{2+}-activated K^+; NaK, Na^+/K^+ pump; NCX, Na^+/Ca^{2+} exchange; PMCA, plasma membrane Ca^{2+} pump; SERCA, ER Ca^{2+} ATPase; SK, small-conductance K_{Ca}; TCA, tricarboxylic acid.

The Rockefeller University Press $30.00
J. Gen. Physiol. Vol. 138 No. 1 21–37
www.jgp.org/cgi/doi/10.1085/jgp.201110611

rhythm. Subsequent models elaborated metabolic components by including details of glycolysis, tricarboxylic acid (TCA) cycle, and oxidative phosphorylation (Magnus and Keizer, 1998; Bertram et al., 2004; Diederichs, 2006) to examine the gating of I_{KATP} by time-dependent changes in [ADP] or glycolytic oscillation. Several models with detailed descriptions of many more membrane currents and associated changes in intracellular ion concentrations have also been published (Miwa and Imai, 1999; Fridlyand et al., 2003; Meyer-Hermann, 2007).

The object of this study is to clarify quantitatively the detailed ionic mechanisms underlying glucose-induced electrical bursting activity observed in isolated β cells. To achieve this aim, we have developed a comprehensive model based on recent extensive experimental findings on ion channels, transporters, and intracellular Ca^{2+} dynamics in β cells. If adequate mathematical analyses are successfully applied to this detailed model, the role of individual ion channels will be clarified in quantitative terms, in relation to the principle mechanisms deduced from the theoretical studies using simplified models, and also in relation to the detailed experimental studies on the role of individual functional molecules in real cells.

MATERIALS AND METHODS

The present model of a single β cell was constructed on the framework developed by Fridlyand, Philipson, and their colleagues, the FP model (Fridlyand et al., 2003, 2005), which was designed to examine interactions among glucose metabolism, Ca^{2+} dynamics including ER, and membrane excitation. The metabolic elements of the model were adopted after minor modifications, whereas the formulations of individual ion channels and transporters were largely revised to reproduce the detailed characteristics of electrical activities reported in the literature. The structure of the model is illustrated in Fig. 1. Because electrical activities or glucose sensitivities vary diversely among different studies or species, we have concentrated on data obtained from dissociated mouse β cells at physiological temperature (33–37°C). Experimental results from other species, including rat and human, or obtained at room temperature were also referred in the absence of relevant mouse data. All equations and parameters are presented in the supplemental material.

Cell dimensions and Ca^{2+} buffer

Cytosolic (764 fl) and ER (280 fl) volumes and membrane capacitance (6.158 pF) were defined as in the FP model (Fridlyand et al., 2003). This capacitance is within the experimental range measured in isolated β cells in mouse (5.4 ± 0.9 pF) (Rorsman and Trube, 1986) and similar to that found in humans (6.2 ± 0.8 or 7.3 ± 0.4 pF) (Kelly et al., 1991). The concentrations of free Ca^{2+} in the cytosol ($[Ca^{2+}]_i$) and ER ($[Ca^{2+}]_{ER}$) were calculated using the buffering power coefficients f_i and f_{ER}, respectively (see Eqs. S5 and S6 in the supplemental material). The value of f_{ER} was determined using the decay time course of the Ca^{2+} transient evoked by a 45-mM K^+ pulse (Gilon et al., 1999), assuming an ER Ca^{2+}-binding capacity of 98–99% as found in gonadotropes (Tse et al., 1994).

Modeling ion channels and transporters

Plasma membrane ion transport comprised eight ion channels and three ion transporters as indicated in Fig. 1. Modeling parameters were based on voltage-clamp data obtained mainly in dissociated β cells, as indicated.

Voltage-dependent Ca^{2+} current (I_{CaV}). It is well established that the maximum rate of rise of action potential is determined by the activation of voltage (V)-dependent Ca^{2+} currents in pancreatic β cells (Ribalet and Beigelman, 1980; Rorsman and Trube, 1986; Ashcroft and Rorsman, 1989). Several types of voltage-gated Ca^{2+} channels (L, R, and possibly P/Q type) have been reported in mouse β cells (Schulla et al., 2003). Braun et al. (2008) also demonstrated that human β cells express L, T, and P/Q types, but not R-type Ca^{2+} channels. At present, it is not possible to describe quantitatively each component because of the lack of detailed voltage-clamp data from isolated cells. However, the whole cell Ca^{2+} currents so far reported show common characteristics for L-type Ca^{2+} current established in other cell types. These include Ca^{2+}-mediated inactivation (Plant, 1988; Satin and Cook, 1989; Kelly et al., 1991), ultraslow V-dependent inactivation (Satin and Cook, 1989; Kelly et al., 1991), and activation by intracellular ATP (Smith et al., 1989) or "washout" with an ATP-free pipette solution (Hiriart and Matteson, 1988). All of these properties might be heavily involved in modulation of membrane excitability. For example, Henquin and Meissner (1984a) ascribed a gradual decrease in the amplitude and frequency of Ca^{2+} spikes to Ca^{2+}- and ultraslow V-dependent inactivation of I_{CaV} during the burst. As an initial approximation, we have used a lumped Ca^{2+} current with characteristics similar to those of L-type Ca^{2+} current described by a formulation of I_{CaL} developed in cardiac myocytes (Takeuchi et al., 2006). The parameters were adjusted according to voltage-clamp experiments in an insulin-secreting cell line (Satin and Cook, 1989; see Fig. S1) and in isolated mouse β cells (Houamed et al., 2010). Because the kinetics of Ca^{2+} current of human β cells are

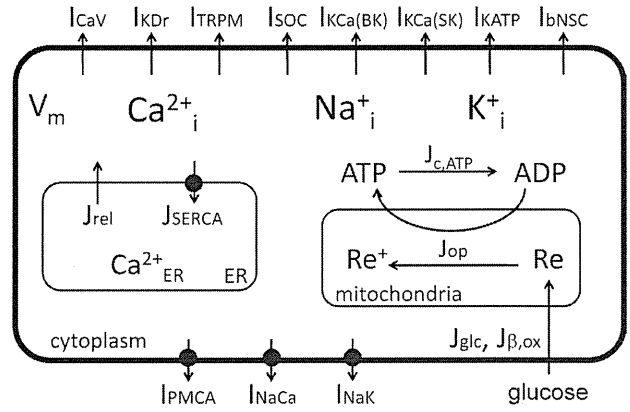

Figure 1. Schematic diagram of the new β-cell model. The model includes ion fluxes through the plasma membrane, Ca^{2+} dynamics including the ER, and [G]-dependent ATP synthesis in mitochondria. The ion fluxes include voltage-dependent Ca^{2+} current (I_{CaV}), delayed rectifier K^+ current (I_{KDr}), Ca^{2+}-activated nonselective cation current (I_{TRPM}), store-operated current (I_{SOC}), V- and $[Ca^{2+}]_i$-dependent transient outward K^+ current ($I_{KCa(BK)}$), ATP-sensitive K^+ current (I_{KATP}), Ca^{2+}-activated K^+ current ($I_{KCa(SK)}$), background nonselective cation current (I_{bNSC}), PMCA current (I_{PMCA}), NCX current (I_{NaCa}), and NaK current (I_{NaK}). ER Ca^{2+} dynamics consist of Ca^{2+} uptake by SERCA (J_{SERCA}) and Ca^{2+} release (J_{rel}). In the ATP synthesis pathway, Re represents the reduced form of pyridine nucleotide (NADH), and J_{glc} and $J_{\beta,ox}$ represent the glycolysis- and β oxidation–dependent Re production rates, respectively. ATP is synthesized at the expense of Re through oxidative phosphorylation (J_{op}) and is consumed via Ca^{2+}-dependent/-independent pathways ($J_{c,ATP}$). The direction of arrows indicates the positive sign of the values calculated by the corresponding equations in the supplemental material.

similar to those in rodent (Kelly et al., 1991), human data were also used for determining the voltage-dependent activation curve and the time course of ultraslow inactivation. Ca^{2+}-dependent inactivation was described as a function of the single-channel current (Eqs. S18 and S19). For ultraslow inactivation, a noninactivating fraction of 0.4 (Eq. S13) was assumed to reproduce the inactivation curve obtained with a 10-s conditioning pulse (Fig. S1 F). Ideally, all of these properties might better be systematically analyzed in a single study at the physiological temperature. Such a study is awaited.

Delayed rectifier K^+ current (I_{KDr}). Pancreatic β cells show a marked delayed outward K^+ current on depolarization (Cook and Hales, 1984; Rorsman and Trube, 1986; Smith et al., 1990b). The voltage-clamp record of I_{KDr} in dissociated β cells of mouse (Houamed et al., 2010) was reproduced (Fig. S2, A and B). For a more precise description of the activation gate (Eqs. S26 and S27), the I-V relationship and activation curve obtained from human (Kelly et al., 1991) and mouse β cells (Rorsman and Trube, 1986) were also considered (Fig. S2 C). In addition, a slow inactivation of I_{KDr} has been observed in various studies (Rorsman and Trube, 1986; Kelly et al., 1991; Houamed et al., 2010). Because the inactivation kinetics were highly dependent on temperature (MacDonald et al., 2003), a time constant of ~0.3 s at +10 mV at 32–35°C (Houamed et al., 2010) was used for model adjustment (Eqs. S29 and S30).

Ca^{2+}-activated nonselective cation current (I_{TRPM}). Sturgess et al. (1987) recorded single-channel currents of a Ca^{2+}-activated nonselective cation channel in the INS-1 cell line. Recently, an analogous but more specific current has been described as a TRPM4 channel current, which might be involved in insulin secretion (Cheng et al., 2007; Marigo et al., 2009). In spite of the recent findings, this channel has not been implemented in previous β-cell models. We described the activation by Ca^{2+} (Eq. S48) with a half-saturation concentration (0.76 μM) and a Hill coefficient (1.7), consistent with experimental recordings (Marigo et al., 2009). The relative permeabilities of Na^+ and K^+ (Eqs. S50 and S51) were adjusted to give a reversal potential of ~0 mV (Colsoul et al., 2010). The whole cell conductance of I_{TRPM} was adjusted to reconstruct the plateau potential of approximately −50 mV during the burst.

Store-operated current (I_{SOC}). Worley et al. (1994a,b) showed that depletion of ER Ca^{2+} store by zero Ca^{2+} bath solution with EGTA depolarized the membrane in freshly isolated mouse β cells. They also demonstrated that a nonselective cation current was activated by maitotoxin. Leech and Habener (1998) also recorded a similar maitotoxin-sensitive current that showed a reversal potential of −1.7 mV in insulinoma cell lines. The authors suggested that this current might play a critical role in setting the membrane potential (V_m) to be less negative than the K^+ equilibrium potential. Unfortunately, it is still unknown if the store-operated cation currents are attributable to a single class of ion channels at the molecular level. Moreover, the critical level of ER Ca^{2+} depletion for the half-activation of the store-operated currents ($K_{0.5,ER}$) remains unclear in β cells. Although a Ca^{2+} release–activated nonselective cation (CRAN) current has been implemented in previous β-cell models (Bertram et al., 1995a; Chay, 1996, 1997; Mears et al., 1997; Fridlyand et al., 2003), different values of $K_{0.5,ER}$ ranging from 3 to 200 μM were used. In our model, the minimum level of 3 μM $[Ca^{2+}]_{ER}$ is tentatively assumed for the half-activation (Eq. S44). With this assumption, the amplitude of I_{SOC} is minimum under the physiological conditions, but it is activated when the ER is almost completely depleted, for example, by applying thapsigargin.

Miura et al. (1997) demonstrated that depletion of Ca^{2+} store by thapsigargin triggered Ca^{2+} influx independent of I_{CaV}, which might be attributed to a different type of current from I_{CRAN}. Based on their finding, I_{SOC} in our model is partly carried by Ca^{2+}, and the size of the current was determined by the steady-state level of $[Ca^{2+}]_i$ under thapsigargin and D_{600}, a blocker of I_{CaV} (Eq. S47). It is consistent with the fact that ubiquitous Ca^{2+} release–activated Ca^{2+} (CRAC) channels are selective to Ca^{2+} under physiological ionic conditions (Hoth and Penner, 1993; Prakriya and Lewis, 2002). This Ca^{2+} entry prevents ER from a serious depletion at 0 mM [G] in our model, and the Na^+ and K^+ conductance of I_{SOC} sets the resting membrane potential at approximately −70 mV in competition with the background of I_{KATP} (Eqs. S45 and S46).

V- and $[Ca^{2+}]_i$-dependent transient outward K^+ current ($I_{KCa(BK)}$). A large-conductance Ca^{2+}-activated K^+ (BK) current has been recorded in single-channel recordings in insulin-secreting cell lines and mouse β cells (Velasco and Petersen, 1987; Satin et al., 1989; Kukuljan et al., 1991; Houamed et al., 2010). Smith et al. (1990b) found that the amplitude of the whole cell outward current was not affected by chelation of intracellular Ca^{2+} by adding [EGTA] to pipette solutions, but they observed that a transient component was depressed by blocking I_{CaV}. Furthermore, single-channel recordings demonstrated that this current was activated immediately after the onset of a depolarizing pulse. These findings suggested that the channel might be functionally coupled to Ca^{2+} channels rather than to bulk cytosolic $[Ca^{2+}]$. Similar transient outward currents coupled with I_{CaV} have also been reported in human β cells (Herrington et al., 2005; Braun et al., 2008). Because it is difficult to estimate $[Ca^{2+}]$ near the BK channel molecule, this current was tentatively represented as a V-dependent transient K^+ current based on the above properties (Eqs. S32–S37). The rate constants for activation and inactivation were determined based on the measurement in dissociated mouse β cells at 33.5°C (Houamed et al., 2010). It has been suggested that this current is a major determinant of the action potential amplitude (Henquin, 1990; Braun et al., 2008; Houamed et al., 2010; Jacobson et al., 2010). Thus, the conductance of $I_{KCa(BK)}$ was determined to set an action potential peak from −10 to 0 mV (Eq. S31).

ATP-sensitive K^+ current (I_{KATP}). It has been well established that the open probability of ATP-sensitive K^+ channel changes depending on the intracellular energy status (Cook and Hales, 1984; Rorsman and Trube, 1985), and thereby I_{KATP} modulates membrane excitability and subsequent insulin secretion in β cells (Larsson et al., 1996). Hopkins et al. (1992) suggested that the channel activity is dependent on ADP level over the concentration range of 10–100 μM, rather than on the ATP/ADP ratio (Dunne and Petersen, 1986; Misler et al., 1986). Based on a reaction scheme with two ADP-binding sites (Hopkins et al., 1992), Magnus and Keizer (1998) proposed a detailed model of I_{KATP}. We adopted this model after a minor modification of dissociation constants for ATP and MgADP according to experimental data (Ashcroft and Kakei, 1989; Hopkins et al., 1992).

Rorsman and Trube (1985) found that the input conductance was ~0.05 nS (20 GΩ in the input resistance) at 10 mM [G], but it increased to 1.9 ± 0.1 nS/pF when ATP was omitted from the intracellular solution. Subsequently, Smith et al. (1990a) observed a similar increase of input conductance to 5.1 ± 0.9 nS under 0 mM [G], which was almost completely inhibited by tolbutamide, a selective K_{ATP} channel blocker. Because these data could constrain the maximum conductance of I_{KATP} (G_{KATP}; Eq. S53) in our model, we simulated a corresponding measurement with a voltage-clamp step from −70 to −80 mV. The whole cell input conductance ranged from 0.048 to 0.068 nS during bursting rhythm at 10 mM [G], which was in good agreement with the experimental value

(Rorsman and Trube, 1985). Under zero intracellular ATP, however, the input conductance only increased to 0.9 nS, >90% of which was attributed to K_{ATP} conductance. This value was much smaller than the experimental measurements. However, we failed to improve G_{KATP} of the original model of I_{KATP} (Magnus and Keizer, 1998), and this problem was left for future work.

Ca^{2+}-activated K^+ current ($I_{KCa(SK)}$). In islet preparations, Göpel et al. (1999a) recorded a novel K^+ current component (I_{Kslow}), which was activated with a slow time constant of ~2.3 s during a train of depolarizing pulses and deactivated with a time constant of 6.5 s after the pulses. An analogous current was also recorded in dispersed mouse β cells in several studies (Göpel et al., 1999a; Goforth et al., 2002; Zhang et al., 2005; Düfer et al., 2009). The pharmacological and gene knockout studies have suggested that small-conductance K_{Ca} (SK) channels might contribute substantially to I_{Kslow} (Zhang et al., 2005; Düfer et al., 2009). Supporting this view, isoforms of SK −1 to −4 were found to be expressed at the level of mRNA and protein in mouse β cells (Tamarina et al., 2003; Düfer et al., 2009). Interestingly, Kanno et al. (2002) ascribed ~50% of the experimental I_{Kslow} to I_{KATP}. Thus, we implemented the SK channel current as $I_{KCa(SK)}$ in our new model separately from I_{KATP}. The Ca^{2+} dependency for activation of $I_{KCa(SK)}$ was adopted from Hirschberg et al. (1998) (Eq. S38). It seems that the activation by Ca^{2+} of SK current is almost instantaneous, but slow changes in $[Ca^{2+}]_i$ and/or the contaminated I_{KATP} component might result in the slow time course of I_{Kslow} in experimental recordings.

Background nonselective cation current (I_{bNSC}). Henquin and Meissner (1984a) showed that the resting membrane potential of β cells is less negative than the K^+ equilibrium potential. They attributed this depolarizing effect to a basal membrane Na^+ conductance (see also Ashcroft and Rorsman, 1989). It is now well established that this background Na^+ conductance includes several types of currents. Nevertheless, a background cation current is still required to establish the resting potential, especially when I_{CRAN} is largely inactivated. Thus, we added such a current, I_{bNSC}, of an unspecified nature. Note that many previous β-cell models also included a background current component (Chay and Keizer, 1983; Chay, 1996; Magnus and Keizer, 1998; Meyer-Hermann, 2007; Fridlyand et al., 2009). I_{bNSC} in this model is permeable to Na^+ and K^+ with a reversal potential at approximately −20 mV (Eqs. S40–S42). The conductance was adjusted to give both the resting membrane potential and input impedance consistent with experimental measurements at a low [G] (Rorsman et al., 1986; Rorsman and Trube, 1986).

Plasma membrane Ca^{2+} pump (PMCA) and Na^+/Ca^{2+} exchange (NCX) currents (I_{PMCA}, I_{NaCa}). Ca^{2+} influx through I_{CaV} is balanced with Ca^{2+} efflux via I_{PMCA} (PMCA1, 2, and 3) and I_{NaCa} (NCX1) (Váradi et al., 1995; Herchuelz et al., 2007). PMCA has one Ca^{2+}-binding site and 1:1 Ca^{2+}/ATP stoichiometry (Brini and Carafoli, 2009). PMCA2 has an apparent Hill coefficient of ~2 (Caride et al., 2001) and the half-maximal concentration of ~0.1 μM $[Ca^{2+}]_i$ in the presence of calmodulin (Enyedi et al., 1991; Elwess et al., 1997). Based on these findings, I_{PMCA} is expressed by a Hill equation (Eq. S95). In addition, it is known that PMCA exchanges one intracellular Ca^{2+} for one extracellular H^+ (Hao et al., 1994), and we assumed that the excess H^+ was instantaneously removed by Na^+/H^+ exchange. Because Na^+/H^+ exchange was not included in the present model, the resultant Na^+ influx by the functional coupling of PMCA and Na^+/H^+ exchange was directly included in calculating $d[Na^+]_i/dt$ (Eq. S3).

The description of I_{NaCa} was adopted from a cardiac myocyte model (Takeuchi et al., 2006), which describes time-dependent transitions between different functional states of the NCX molecule (Eqs. S75–S94). The slope conductance of I_{NaCa} near the reversal potential was 25.5 pS pF^{-1} at 14 μM $[Ca^{2+}]_i$ and 30 mM $[Na^+]_i$ in the present model, which is about half of the experimental value (53 pS pF^{-1}) (Gall et al., 1999). This difference seems to fall within the range of experimental variations because of the limited intracellular perfusion with pipette solutions through the ruptured patch.

NaK current (I_{NaK}). The I_{NaK} model was adopted from Oka et al. (2010), in which the turnover rate was precisely described in terms of V_m, intracellular, and extracellular compositions of Na^+ and K^+, and the free energy of ATP hydrolysis (ΔG_{ATP}) based on thermodynamics (Eqs. S54–S74). Although this model was developed with reference to experimental measurements in cardiac myocytes, we assumed for convenience that the basic characteristics of the pump activity would be common in β cells. In addition, the inhibition of the pump activity by glucose via intracellular signaling (Owada et al., 1999) was implemented (F_{glc}; Eq. S55). The amplitude factor of I_{NaK} (P_{NaK}) was determined to satisfy Na^+ homeostasis in both quiescent and bursting activities. Finally, the K^+ balance between efflux through K^+ channels and the active influx via NaK was calculated, rather than fixing $[K^+]_i$ as in the original FP model.

Modeling intracellular Ca^{2+} dynamics

A precise description of ER Ca^{2+} dynamics is critical for modeling β-cell function. Uptake of Ca^{2+} into the ER is mediated by ER Ca^{2+} ATPase (SERCA), and approximately equal amounts of SERCA 2b and 3 are expressed in pancreatic islets (Váradi et al., 1996). The apparent affinity for cytosolic Ca^{2+} was determined with a half-activation concentration ($K_{1/2}$) of 0.27 and 1.1 μM, and a Hill coefficient (n^H) of 1.7 and 1.8 for SERCA 2b and 3, respectively (Lytton et al., 1992). The SERCA activity in the present study was represented with a Hill equation of $K_{1/2} = 0.5$ μM and $n^H = 2$, compromised for the whole cell simulation (Eq. S96). Ca^{2+} release from ER is a critical determinant for reconstructing the slow decay phase of $[Ca^{2+}]_i$ observed after action potential burst. Although an application of IP_3 facilitates Ca^{2+} release (Tengholm et al., 2001), the slow Ca^{2+} decay during the interburst did not seem to be triggered by IP_3-, depolarization-, nor Ca^{2+}-induced Ca^{2+} release (Gilon et al., 1999). Therefore, ER Ca^{2+} release (J_{rel}) was described as a passive flux down a concentration gradient in this study (Eq. S97).

ER volume (vol_{ER}), maximum velocity of SERCA (P_{SERCA}; Eq. S96), nor the permeability of the Ca^{2+} release channel (P_{rel}; Eq. S97) has been fully measured to provide definite values of these parameters. Thus, they were adjusted based on the following experimental findings. (a) The physiological level of $[Ca^{2+}]_i$ hardly exceeds 0.5 μM during glucose stimulation (Rorsman et al., 1984). (b) The resting $[Ca^{2+}]_i$ is 60–100 nM (Rorsman et al., 1992; Chow et al., 1995). (c) Onset and offset time courses of Ca^{2+} transient were recorded, which were evoked by the action potential burst, a voltage-clamp pulse, or K^+-induced depolarization (Gall et al., 1999; Gilon et al., 1999). (d) Direct measurement of $[Ca^{2+}]_{ER}$ using a low affinity Ca^{2+} fluorescent dye revealed that $[Ca^{2+}]_{ER}$ is maximally increased up to ~200 μM by Ca^{2+} uptake through SERCA in the absence of IP_3 (Tengholm et al., 2001). It was consistent with $[Ca^{2+}]_{ER}$ of 60–200 μM suggested previously (Tse et al., 1994). (e) At 12 mM [G], Ca^{2+}-stimulated ATPase activity of SERCA was comparable to that of PMCA in β cells (Roe et al., 1994). In the present β-cell model, the ratio of ATP consumption by SERCA and PMCA was approximately 1:1 at 12 mM [G], ranging from 1:3 in a quiescent state at 6 mM [G] to 4:3 during continuous firing at 20 mM [G].

Modeling energy metabolism

Fridlyand et al. (2005) elaborated a set of equations for ATP production through glycolysis and oxidative phosphorylation, and for ATP consumption based on a wide range of biochemical studies. We used their model with a few modifications as follows. First, we changed the glucose dependency of glycolysis (f_{glc}) (Eq. S100) to reproduce the experimental finding that the burst duration is prolonged with increasing [G] in β cells. Our revision might be appropriate because f_{glc} reflects the [G] dependency of all the reaction steps including glycolysis and TCA cycle in our model. Note that the original values in the FP model were determined under the assumption that glucose phosphorylation by glucokinase was the only limiting step in glycolysis. Second, we calculated ATP production via β oxidation of fatty acid ($J_{\beta,ox}$; Eq. S99), in addition to glycolysis (J_{glc}; Eq. S98). This modification prevented the system from a metabolic collapse at a low [G] (<2 mM), which actually occurred in the FP model. Third, in the production of reduced metabolic compounds (Re), we took account of the total amount of pyridine nucleotides ([Re_{tot}]) by adding a term of ([Re_{tot}] − [Re]) in J_{glc} and $J_{\beta,ox}$ (Eqs. S98 and S99). This term was crucial to avoid an unlimited increase of [Re] at a high [G] (>15 mM), observed in the FP model. Under the assumption that most Re consists of NADH in the mitochondria, [Re_{tot}] of 10 mM was used (Cortassa et al., 2003). The consumption of [Re] by oxidative phosphorylation was calculated using a stoichiometry of 2.5 between ATP and NADH, and with a volume ratio (2.5) between the cytosol and mitochondria (Eq. S102).

Lead potential (V_L) analysis

To clarify the ionic mechanisms underlying burst–interburst rhythm in our new β-cell model, we applied the V_L analysis developed by Cha et al. (2009). The method quantifies the contributions of individual membrane currents to changes in V_m by calculating an equilibrium potential at each moment (V_L) using the time-varying conductance (G_X), reversal potential (E_X), and V-independent transporter current (I_Y),

$$V_L = \frac{\sum_X G_X E_X - \sum_Y I_Y}{\sum_X G_X}. \quad (1)$$

Also refer to Eq. S108. V_L always moves in advance of V_m, and its time derivative (dV_L/dt) drives the automatic change of V_m. The relative contribution (r_c) of a current component of interest (i) is defined by a relative change in dV_L/dt when the time-dependent change of i is selectively fixed. The total sum of r_c for all components equals unity at each time point, and is used to validate the calculations,

$$r_{c,i} = \frac{\frac{dV_L}{dt} - \frac{dV_{L\_Fix,i}}{dt}}{\frac{dV_L}{dt}} \text{ and } \sum_i r_{c,i} = 1. \quad (2)$$

This method has been verified in various cardiac cell models (Cha et al., 2009; Himeno et al., 2011). In the present study, the contribution c (mV s^{-1}) was used, instead of r_c. c was newly defined by the following equation:

$$c_i = \frac{dV_L}{dt} - \frac{dV_{L\_Fix,i}}{dt} \text{ and } \sum_i c_i = \frac{dV_L}{dt}. \quad (3)$$

c with a positive sign indicates that the corresponding component contributes to membrane depolarization, and vice versa.

Among the three electrogenic ion transporters, V-independent I_{PMCA} was treated as a current source (Eq. S108). I_{NaK} and I_{NaCa} were expressed with Eqs. 4 and 5, where G_{NaK} and G_{NaCa} are the slopes of tangential lines fitted to the instantaneous I-V relation at each moment, and E_{x_NaK} and E_{x_NaCa}, the intersections of the tangential lines with the x axis:

$$I_{NaK} = G_{NaK}(V_m - E_{x\_NaK}) \quad (4)$$

$$I_{NaCa} = G_{NaCa}(V_m - E_{x\_NaCa}). \quad (5)$$

The contribution of I_{NaK} or I_{NaCa} in Fig. 5 was a summation of c evaluated by fixing G_{NaK} and E_{x_NaK}, or G_{NaCa} and E_{x_NaCa}, respectively. Because G_{NaK} and E_{x_NaK} are functions of $[Na^+]_i$, $[K^+]_i$, [ATP] or [MgADP], and V_m, the contribution of each concentration change was also evaluated in the bottom panels of Fig. 5.

Online supplemental material

Equations, parameters, and the definition of symbols of the β-cell model are provided in the supplemental material. Table S1 lists the initial values of the 18 variables in this model. Figs. S1 and S2 show reconstructions of I_{CaV} and I_{KDr} in voltage-clamp experiments, respectively. Fig. S3 shows the effect of thapsigargin on the Ca^{2+} transients induced by applying high K^+ pulses to the model. Fig. S4 is V_L diagram of the FP model for comparison to our model (Fig. 5). The supplemental material is available at http://www.jgp.org/cgi/content/full/jgp.201110611/DC1.

RESULTS

Electrical activity and intracellular concentrations of ions and metabolites in pancreatic β cells

Burst of action potentials evoked by various glucose concentrations. Fig. 2 shows the time-dependent changes in V_m, [ATP], [MgADP], $[Na^+]_i$, and $[Ca^{2+}]_i$ evoked by different [G] in the new β-cell model. At [G] < 6 mM, the membrane was quiescent, and the concentrations of intracellular ions and metabolites remained at various steady-state levels depending on [G]. The resting potential decreased from −70 mV at 0 mM [G] (not depicted) to −58 mV at 6 mM [G], accompanied by an increase in the input impedance from 4 to 15 GΩ. This input impedance is comparable to experimental measurements of 3–30 GΩ (Rorsman and Trube, 1986), 1–10 GΩ (Rorsman et al., 1986), or 3 GΩ (Smith et al., 1990a). In the simulation, the increase in input impedance largely resulted from the progressive closure of I_{KATP} channels. At 7 mM [G], a typical burst of action potentials appeared. The burst duration was elongated as [G] increased, and finally the burst was transformed to a continuous firing at [G] > 19 mM (Ashcroft et al., 1984; Henquin and Meissner, 1984b). The interburst phase is also elongated at a higher [G] in the present study because more time was required to recover from ion accumulation during the preceding burst period of longer duration. This simulation result is in agreement with the experimental data from mouse islets showing longer burst and interburst periods at a higher [G] (Antunes et al., 2000). Our model, however, failed to reconstruct gradual shortening of the interburst period with [G] (Meissner and Schmelz, 1974).

The action potential in the model is in good agreement with the representative burst activity recorded in a single β cell in the presence of 2.6 mM $[Ca^{2+}]_o$ and 10 mM [G] at 31°C (see Fig. 1 B in Smith et al., 1990a). The maximum rate of rise was 2–3 V s^{-1} in the model, comparable to 3.2 V s^{-1} (Rorsman and Trube, 1986) or 3.5 V s^{-1} (Dean et al., 1975). The peak potential was about −4 mV in the model versus −8.3 mV experimentally (Smith et al., 1990a), the plateau potential was about −50 versus −53.7 mV, and the maximum negative potential during the interburst period was about −68 versus −76.4 mV. The maintenance of the plateau potential was mainly attributable to I_{CaV} conductance remaining at the end of the action potentials. It was supported by a simulation showing that the burst was interrupted if I_{CaV} was instantaneously deactivated by applying a brief hyperpolarizing voltage pulse (not depicted). The Ca^{2+}-activated inward currents, I_{TRPM} and I_{NaCa}, also contributed to the maintenance of the plateau potential.

Slow fluctuations in [ATP], [MgADP], $[Na^+]_i$, and $[Ca^{2+}]_i$ during burst–interburst rhythm. In our model, [ATP] and [MgADP] changed in synchrony with electrical events at [G] > 7 mM (Fig. 2, second row). That is, [MgADP] increased at the expense of ATP during the burst and in turn decreased during the subsequent quiescent period when the cell was relieved from the extra Ca^{2+}-dependent ATP consumption. These typical responses were observed at 8 mM [G]. At 12 or 16 mM [G], however, the ATP consumption was compensated for to a greater extent by increased ATP production. Thus, [MgADP] increased much slower during the burst, and its maximum level at the end of burst was lower in spite of the elongated burst duration. On the other hand, the fluctuation in $[Na^+]_i$ was enlarged with an increase in burst duration, and finally $[Na^+]_i$ remained elevated at [G] > 19 mM (Fig. 2). Accumulation of $[Na^+]_i$ was mostly a result of Na^+ influx through NCX, which compensated for the large Ca^{2+} influx through I_{CaV}. Based on the opposite changes in the fluctuations of [ATP] and $[Na^+]_i$ by increasing [G], our β-cell model predicted that the activation of I_{NaK} by the accumulation of $[Na^+]_i$ might take over the role of I_{KATP} in terminating the burst at a higher [G].

Fluctuation in $[Ca^{2+}]_i$ during the burst–interburst rhythm also has profound effects on the electrical activity. As demonstrated in Fig. 2, $[Ca^{2+}]_i$ jumped from a resting level of ~100 to ~400 nM at the onset of the burst, and then the plateau level of the oscillation (fast Ca^{2+} ripple) slowly decreased during the burst, because of the slow inactivation of I_{CaV}. At [G] > 12 mM, a brief oscillation in the plateau level of the Ca^{2+} ripple preceded the final termination of the burst, which has not been described by experimental studies. We found that this oscillation was sensitive to the amplitude of $I_{KCa(SK)}$ but failed to clarify the underlying mechanisms in the present study. After cessation of the burst, a slow decay

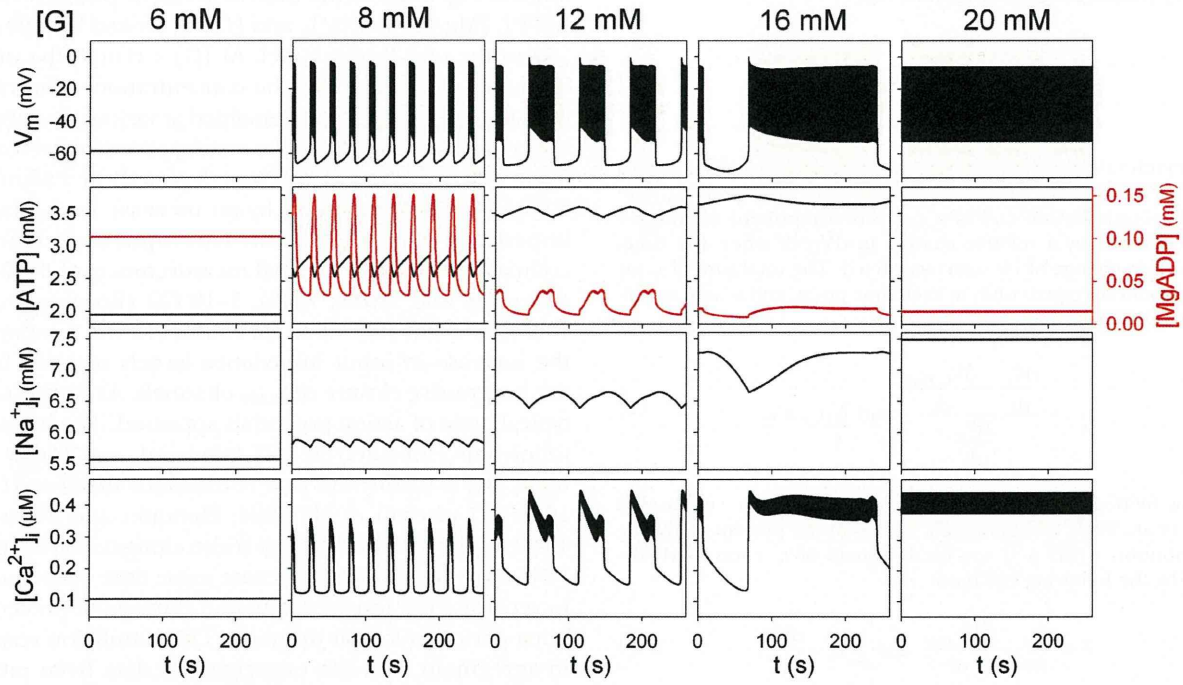

Figure 2. Activities of the β-cell model at various [G]. Each row indicates steady cyclic changes in V_m, [ATP] (black), [MgADP] (red), $[Na^+]_i$, and $[Ca^{2+}]_i$ in the presence of 8, 12, and 16 mM [G], or a quiescent state at 6 mM [G] and continuous firing of the action potentials at 20 mM [G]. All records were obtained with initial values in Table S1 after the rhythm of the cyclic events became stable after switching [G].

phase (or Ca^{2+} tail) was observed at 12 and 16 mM [G], but hardly at 8 mM [G]. This Ca^{2+} tail is caused by release of Ca^{2+} from the ER, which has accumulated during the preceding burst. The increase in the Ca^{2+} fluctuation at a higher [G] has complex influences on membrane ion channels or transporters, that is, activation of outward-going I_{PMCA} or $I_{KCa(SK)}$, as well as inward-going I_{NaCa} or I_{TRPM}. The overall effects of $[Ca^{2+}]_i$ will be evaluated mathematically later.

Role of ER Ca^{2+} dynamics in glucose-induced burst–interburst rhythm

Ca^{2+} dynamics in the new β-cell model were validated before we analyzed the ionic mechanisms. In control conditions, a regular burst–interburst rhythm and the accompanying Ca^{2+} transients were generated with a cycle length of ~40 s at 11 mM [G] (Fig. 3, the left half). At the onset of a burst, most Ca^{2+} influx through I_{CaV} was instantaneously captured by cytosolic Ca^{2+}-binding proteins (f_i in Eq. S5). Then, during the initial 1 s of the burst, the Ca^{2+} influx was compensated for by the ER (J_{SERCA}-J_{rel}; 44%), PMCA (26%), and NCX (34%) (Fig. 3, bottom), which was in good agreement with experimental results (Gall et al., 1999). As the burst progressed, Ca^{2+} gradually accumulated in the ER, and thus the ER Ca^{2+}-buffering capacity became less effective because of an increase in Ca^{2+} release from the ER. Importantly, 97% of the Ca^{2+} accumulated during the whole burst was taken up by the ER, and only 3% remained in the cytosol. After cessation of the burst, the accumulated Ca^{2+} in the ER was slowly released into the cytosol (Fig. 3, bottom), which is a main contributor of the long-lasting Ca^{2+} tail. This simulation result is in line with experimental responses (Gilon et al., 1999).

For further examination of the relevance of the Ca^{2+} dynamics in the model, the effects of blocking SERCA by thapsigargin were simulated. In the right half of Fig. 3 indicated by a gray horizontal bar, the activity of SERCA was reduced to 20% of the control. As a result, the Ca^{2+}-buffering capacity of ER decreased, and in the steady state, the amplitude of Ca^{2+} oscillation was increased by nearly two times. In addition, the Ca^{2+} tail disappeared from the interburst period and the electrical rhythm became about two times faster through the shortening of both interburst and burst periods. These findings are in good agreement with several experimental recordings (Miura et al., 1997; Gilon et al., 1999; Fridlyand et al., 2003) and previous simulation results (Fridlyand et al., 2003; Bertram and Sherman, 2004). The rate of depolarization during the interburst was accelerated by the activation of inward I_{SOC} as a result of ER depletion. The burst duration was also reduced because the opening of I_{KATP} was accelerated by the enhanced Ca^{2+}-dependent ATP consumption. Increased outward $I_{KCa(SK)}$ or I_{PMCA} by the amplified Ca^{2+} transient might also help the early termination of the burst, whereas inward I_{NaCa} and I_{TRPM} have the opposite effects.

We also simulated Ca^{2+} transients induced by applying 45 mM of K^+ solution (Fig. S3). The Ca^{2+} tail observed after the high K^+ pulse was well reconstructed (Gilon et al., 1999). The simulation predicted that $[Ca^{2+}]_{ER}$ was accumulated up to ~60 μM via I_{CaV} activated through high K^+-induced depolarization (approximately −25 mV). In the presence of thapsigargin, the amplitude of Ca^{2+} transients was increased with a large initial peak, and the slow Ca^{2+} tail disappeared. The slow inactivation of I_{CaV} caused the marked decrease in $[Ca^{2+}]_i$ during the initial 10 s of the pulse, as well as the temporal depression after washing out the high K^+ solution.

Ionic mechanisms underlying the electrical activity of β cells

Current profile during the burst and interburst periods. The findings in Fig. 2 suggested that the burst rhythm is determined by the balance among current components

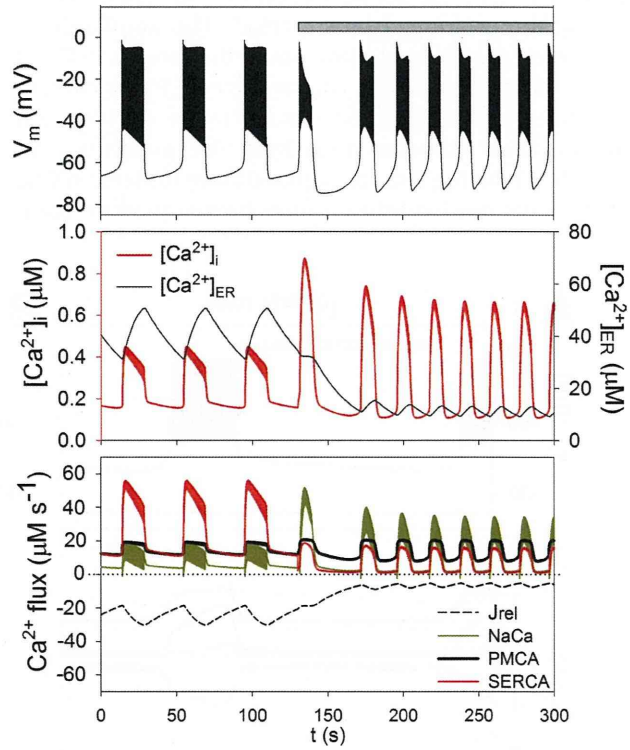

Figure 3. Dynamics underlying spontaneous Ca^{2+} oscillations before and after inhibition of SERCA. Time-dependent changes in V_m (top), and $[Ca^{2+}]_i$ and $[Ca^{2+}]_{ER}$ (middle), and Ca^{2+} fluxes through J_{rel}, J_{SERCA}, I_{NaCa}, and I_{PMCA} (bottom) at 11 mM [G] are illustrated with different colors, as indicated in each panel. The scale of $[Ca^{2+}]_{ER}$ is represented on the right y axis (middle), and the zero flux level is indicated by a dotted line (bottom). From 130 s (gray horizontal bar), P_{SERCA} was reduced to 20% of its control value (from 0.096 to 0.0192 amole ms^{-1}) to simulate the blocking effect of SERCA by thapsigargin. The net Ca^{2+} flux through the ER was calculated by subtracting J_{rel} from J_{SERCA}.

that are modulated by slow changes in [ATP] and [MgADP], as well as those in $[Na^+]_i$ and $[Ca^{2+}]_i$. We measured the amplitudes of all these currents, including I_{KATP}, I_{NaK}, I_{NaCa}, I_{PMCA}, I_{TRPM}, and $I_{KCa(SK)}$, at 8 and 16 mM [G], in addition to V-dependent I_{CaV} and I_{KDr} (Fig. 4). During the burst period, the current levels were measured at the most negative potential between successive action potentials. The plateau potential gradually shifted negative toward the threshold for the full repolarization of the burst termination. At both [G], I_{KDr} was of minimum size because of almost complete deactivation at the end of individual action potentials, and its contribution to changing the plateau potential seemed to be negligible. In contrast, I_{CaV} had the largest amplitude, suggesting that it is the major current maintaining the plateau potential or driving the interburst depolarization to trigger the subsequent action potential burst. I_{KATP} provided a sizable outward current during the interburst at 8 mM [G] but was much decreased at 16 mM [G]. In contrast, outward I_{NaK} and $I_{KCa(SK)}$, and inward I_{NaCa} and I_{TRPM}, were substantially increased at 16 mM [G] by the accumulation of $[Na^+]_i$ and $[Ca^{2+}]_i$ during the prolonged burst period. The amplitude of I_{SOC} was negligibly small throughout the records in Fig. 4 at both 8 and 16 mM [G] (not depicted). These current profiles, however, only give clues as to the contribution of individual currents underlying the generation of electrical bursting activity. A quantitative understanding of the ionic mechanisms requires further mathematical analysis, such as V_L analysis in the next section or bifurcation analysis as described in our companion paper (see Cha et al. in this issue).

V_L analysis of interburst ionic mechanisms. To measure the contribution of each current component to automatic change in V_m, V_L analysis was applied to the simulation results (Eqs. 1, 3, and S108). The magnitudes of the contribution (c in mV s^{-1}; see Materials and methods) of individual ion channels and transporters were calculated over the interburst period, as indicated with horizontal gray bars in Fig. 4 (A and B). c was plotted in a cumulative manner at 8 and 16 mM [G] (Fig. 5, middle panels).

At 8 mM [G], V-dependent activation of I_{CaV} (d_{CaV}), albeit a tiny change from 0.03 to 0.05, provided the largest positive contribution during the entire course of slow depolarization (Fig. 5 A). In contrast, the contribution of ultraslow inactivation of I_{CaV} (f_{us}) was trivial. I_{KATP}, an outward current, also provided a positive contribution to the depolarization ($c \sim 0.1$–0.2 mV s^{-1}) because its open probability was gradually reduced by both increasing [ATP] and decreasing [MgADP]. In the late phase, the contribution of I_{KATP} became smaller by gradual equilibration of [ATP] and [MgADP]. The positive contribution of inward I_{NaCa} ($c < 0.1$ mV s^{-1}) was mainly attributable to increased turnover rate by the gradual decrease of $[Na^+]_i$ after cessation of the burst. I_{NaK}, $I_{KCa(BK)}$, and I_{TRPM} hindered the slow depolarization, as

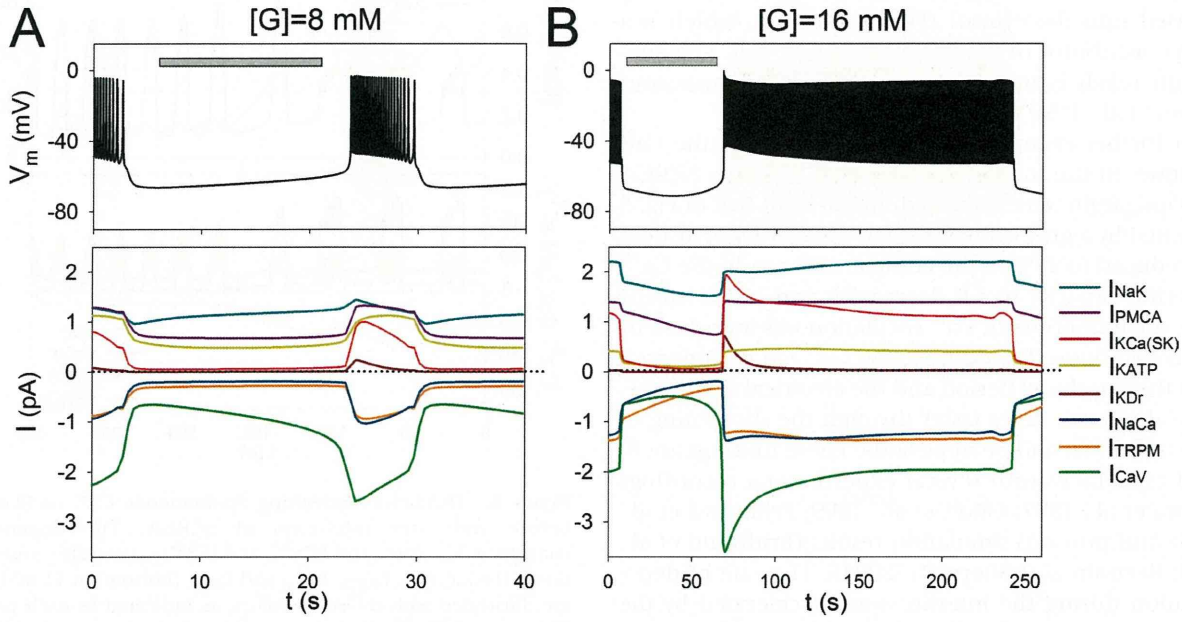

Figure 4. Ionic currents during burst and interburst activity at 8 mM [G] (A) and 16 mM [G] (B). Top panels show V_m and bottom panels show individual ionic currents, with the different colors as indicated on the right. The amplitudes of individual currents were measured at the plateau potential (the most negative potential between successive action potentials) during the burst period. Note that different time scales are used in A and B. The zero current level is indicated by dotted lines. Gray bars indicate the interburst period, where the V_L analysis was applied in Fig. 5.

represented by their negative contributions (less than -0.2 mV s^{-1}).

At 16 mM [G], the ionic mechanisms changed markedly (Fig. 5 B). The contribution of I_{KATP} almost disappeared from the V_L diagram, but the contribution of Ca^{2+}-dependent currents (I_{PMCA}, I_{NaCa}, and I_{TRPM}) noticeably increased in compared with those at 8 mM [G]. The V_m change showed two phases during the interburst period: early hyperpolarization and late depolarization. During the early phase, the hyperpolarization was mainly attributed to decreases in inward I_{NaCa} and I_{TRPM} as a result of the slow decay of $[Ca^{2+}]_i$. The sum of these hyperpolarizing effects was larger than the depolarizing effect caused by the decrease in outward I_{PMCA}. In the late phase, the decay rate of $[Ca^{2+}]_i$ slowed down, the contribution of I_{NaCa} was reversed by the decrease in $[Na^+]_i$, and the negative contribution of I_{TRPM} was also reduced. Furthermore, the decrease in $[Na^+]_i$ gradually reduced outward I_{NaK} and contributed to depolarization. As a consequence, the membrane started to depolarize at the late phase.

Comparison of the V_L diagrams in Fig. 5 (A and B) reveals that a metabolic-dependent mechanism (I_{KATP}) at a lower [G] was replaced by an ion-dependent mechanism (I_{PMCA}, I_{NaCa}, and I_{TRPM}) at a higher [G] in generating the burst–interburst rhythm. This replacement of mechanism was further exemplified by separating the contribution of I_{NaK} into metabolism- and ion-dependent mechanisms (Fig. 5, bottom panels). At 8 mM [G], a negative contribution of I_{NaK} was caused by rapid recovery of the ATP/MgADP composition, whereas at 16 mM [G], the metabolic effects almost disappeared, and the decrease in $[Na^+]_i$ dominated the time course of c of I_{NaK}.

V_L analysis of repetitive action potentials. The result of V_L analysis is presented in Fig. 6 for two successive action potentials during the burst. The V_L (Fig. 6, red line) leads the time-dependent change in V_m (black line) in advance and intersects the V_m curve when dV_m/dt (or I_{tot}) equals zero. The V_L diagram (Fig. 6, bottom) indicates that the time course of the action potential is largely determined by I_{CaV}. In the rising phase of the spontaneous action potential, the progressive V-dependent activation of I_{CaV} plays the major role; likewise, the V-dependent deactivation of I_{CaV} is mainly responsible for repolarization. The activation of $I_{KCa(BK)}$ partially counteracts I_{CaV} to reduce the maximum rate of rise or decay of the action potential. Surprisingly, the delayed activation of outward I_{KDr} provided a negative contribution only at the beginning of the repolarizing phase, but then reversed its contribution to retard the repolarizing influence of I_{CaV}. This retarding effect of I_{KDr} is a result of V-dependent removal of activation (p_{KDr}). The contributions of the other substrate-dependent currents, I_{KATP}, I_{PMCA}, I_{NaCa}, I_{TRPM}, and I_{NaK}, are barely

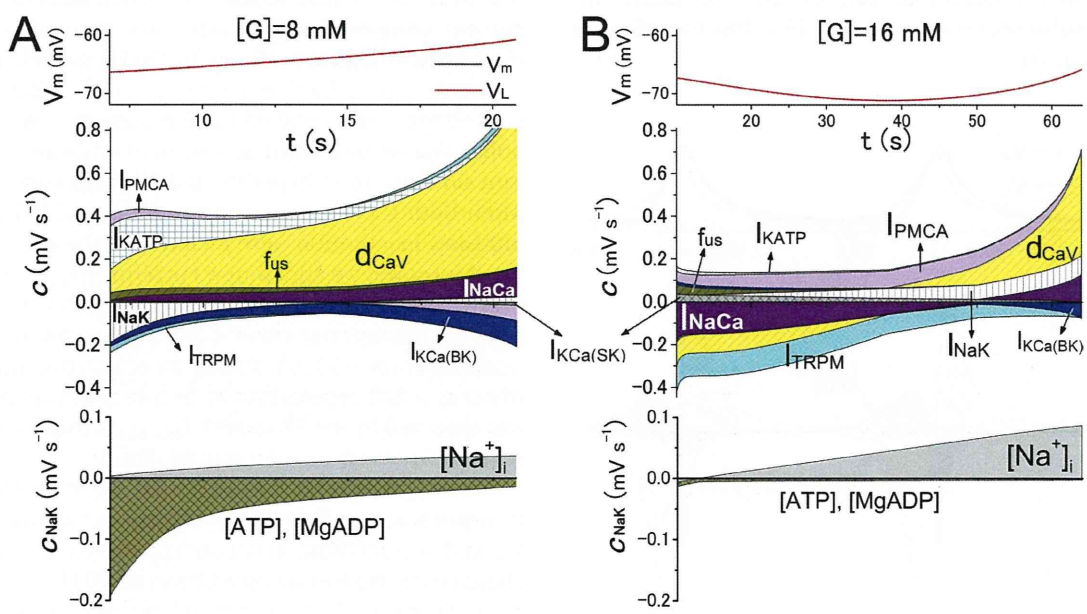

Figure 5. V_L diagrams show the contribution of major currents during the interburst period at 8 mM [G] (A) and 16 mM [G] (B). (Top) Time-dependent changes in V_L (red) and V_m (black). The V_m trace is overlapped by V_L. (Middle) Time-dependent changes in the contribution (c) of individual currents indicated with different colors. A positive c indicates that the time-dependent change in the corresponding current contributes to depolarization (in mV s^{-1}), and vice versa. The contribution of I_{CaV} was divided into c of d_{CaV} and c of f_{us}. The rest for I_{CaV} was negligibly small (not depicted). (Bottom) Separation of the contribution of I_{NaK} into [ATP]- and [MgADP]-dependent components (dark yellow) and $[Na^+]_i$-dependent component (gray). Effects of other factors on I_{NaK}, such as time-dependent changes in $[K^+]_i$ or V_m, were negligibly small (not depicted). The time scales refer to those for the gray bars in Fig. 4 (A and B).

visible because the concentrations of ions or metabolites changed minimally over the time span of an action potential.

An extra effect of [G] on the bursting activity through direct inhibition of NaK

Owada et al. (1999) demonstrated that applying glucose to β cells inhibited Na^+/K^+ ATPase in a dose-dependent and reversible manner via a distinct signal transduction pathway. Because this inhibition was of considerable magnitude (up to 55%), they suggested that the inhibition of I_{NaK} might promote insulin secretion at a high [G]. We tested this hypothesis by switching on the inhibitory action of glucose on I_{NaK} (F_{glc}; Eq. S55) after a steady rhythm was established (Fig. 7). Immediately after I_{NaK} was reduced by introducing the glucose inhibition (Fig. 7, gray bar), an action potential burst of longer duration was evoked accompanied by a larger Ca^{2+} transient, in agreement with the experimental observations using an NaK blocker (Bozem and Henquin, 1988). Contrary to the expectation of Owada et al. (1999), the burst interval returned to control at the next burst and remained constant. The amplitude of I_{NaK} was almost restored because $[Na^+]_i$ gradually increased until I_{NaK} exactly matched the Na^+ influx. The basal level of $[Ca^{2+}]_i$ was initially increased by the intervention but slowly recovered over the next 100 s. Similar results were simulated at 12 mM [G]. The simulation suggests that the partial inhibition of I_{NaK} by glucose might increase insulin secretion at 8 mM [G], but the effect is only transitory.

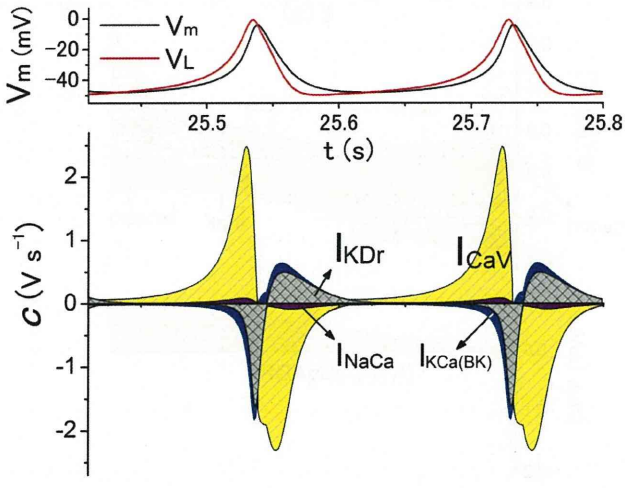

Figure 6. V_L diagram for two successive action potentials within the burst at 8 mM [G]. (Top) Time-dependent changes of V_L (red) and V_m (black). Note that V_L always changes in advance of V_m. (Bottom) Time-dependent changes in contributions (c) of I_{CaV}, I_{KDr}, $I_{KCa(BK)}$, and I_{NaCa}. The c of other currents was also plotted in the diagram but is barely visible because of its minor contributions. The time scale on the x axis refers to that in Fig. 4 A.

DISCUSSION

By integrating a broad range of electrophysiological findings into a mathematical model, the response of pancreatic β cells to extracellular glucose was well reconstructed, and the underlying mechanisms were elucidated in a comprehensive manner. The new β-cell model showed a series of responses to varying [G], that is, the intermittent burst of action potentials accompanied by Ca^{2+} transients at [G] > 7 mM, the elongation of the burst duration with increasing [G], and the continuous firing of action potentials at [G] > 19 mM. V_L analysis of the model successfully quantified contributions of ion channels and transporters to the slow interburst depolarization. It was concluded that alternating burst and interburst events at the physiological range of [G] is regulated mainly by I_{KATP} channels, which transduce signals from varying [ATP] or [MgADP] to membrane excitability. The novel prediction is that the role of I_{KATP} is taken over by electrogenic ion transporters, such as I_{NaCa}, I_{NaK}, I_{PMCA}, and a Ca^{2+}-activated ion channel, I_{TRPM}, at a higher [G].

Comparison with the FP model

To our knowledge, the β-cell model developed by Fridlyand et al. (2003, 2005) provided the first description of individual channels and transporters on a plasma membrane at a molecular level. Our model is based on the structure of this FP model to couple membrane excitation with energy metabolism. We revised most of the ionic current components with reference to more extensive electrophysiological findings. In the FP model, a high K^+ external solution induces continuous Ca^{2+} influx through I_{CaV} (about −30 to −50 pA) and eventually causes a metabolic collapse by a rapid depletion of cytosolic ATP. Relevant simulations to experimental findings were obtained when both Ca^{2+}-mediated inactivation and V-dependent ultraslow inactivation were included in the new model of I_{CaV}. Moreover, we added new currents, I_{TRPM} and $I_{KCa(BK)}$, based on recent experimental findings. We found that I_{TRPM} is an important current to maintain the plateau potential around −50 mV during an action potential burst, whereas a full repolarization between action potentials was observed in the FP model. $I_{KCa(BK)}$ is important in the regulation of action potential amplitude.

For self-consistency of the model, we included all ion transports across the cell membrane in calculating both V_m and intracellular ion concentrations, according to charge conservation law (see Cha et al., 2011). (a) We took account of the H^+ influx via Ca^{2+}/H^+ exchange through PMCA. This H^+ flux was assumed to be completely converted to equivalent Na^+ flux by a fast Na^+/H^+ exchange (see Materials and methods). (b) $[K^+]_i$ was not fixed in our model, but the time-dependent change was calculated by K^+ fluxes through NaK and ion channels. These modifications were prerequisite for examining

the roles of ion transporters, which are greatly affected by ion concentrations.

The model of I_{NaK} in the FP model was largely modified from the original model of Chapman et al. (1983) by omitting state transitions of the carrier protein. This simplification resulted in no saturation of the turnover rate by $[Na^+]_i$. Moreover, I_{NaK} in the FP model is a V-independent current in the range from −80 to 0 mV. We implemented a new kinetic model of I_{NaK} with the state transitions (Oka et al., 2010). It shows properties well established in experimental studies, such as dependencies on Na^+ and K^+, the free energy of ATP hydrolysis (ΔG_{ATP}), and the membrane potential. Thereby, the present study reliably predicted that I_{NaK} took a pivotal role in terminating the burst when $[Na^+]_i$ was accumulated during a long-lasting burst at a high [G] (Fig. 5). For comparison with the present study, we applied V_L analysis to the slow interburst depolarization in the FP model (Fig. S4). At a relatively low [G] (8.5 mM), a V_L diagram demonstrated that the time-dependent decrease of outward I_{NaK} takes the major role in determining the depolarization rate ($c \sim 0.25$ mV s^{-1}), whereas the contribution of I_{KATP} was negligibly small ($c \sim 0.025$ mV s^{-1}). It is because of a relatively rapid production of ATP in the FP model, resulting in a long-lasting burst even at relatively lower [G], accompanied by $[Na^+]_i$ oscillation with an amplitude of ~2 mM.

Mechanisms to generate the bursting activity in modeling studies

Complex patterns of electrical activity in β cells with varying [G] has been one of the interesting targets in the field of mathematical physiology, and several explicit hypotheses have been put forward in various forms of mathematical models. Importantly, however, the fundamental question still remained as to what the slowly varying factor underlying the time course of burst–interburst rhythm in β cells is. Here, we discuss the multiple key membrane components suggested in relation to the slow intracellular factors hypothesized in previous modeling studies, that is, $[Ca^{2+}]_i$, $[Ca^{2+}]_{ER}$, [ATP] and/or [ADP], and $[Na^+]_i$.

$[Ca^{2+}]$ and the Ca^{2+}-activated K^+ currents. One of the major hypotheses assumed a gradual activation of Ca^{2+}-dependent K^+ currents during an action potential burst. For example, early Chay-Keizer models adopted the BK channel (Chay and Keizer, 1983; Sherman et al., 1988), and they predicted that an accumulation of intracellular Ca^{2+} via repetitive spikes increased the outward BK current and terminated the burst. In turn, the burst was resumed when the BK channels were sufficiently deactivated during the interburst period. Distinct from the expectation in their models, however, the progressive accumulation of Ca^{2+} has not been established experimentally, but rather, a rapid rise of the Ca^{2+} transient leveled off to the plateau level within the initial several seconds of the burst (Santos et al., 1991; Worley et al., 1994a), or $[Ca^{2+}]_i$ slightly rose (Gilon and Henquin, 1992; Zhang et al., 2003) or decayed (Miura et al., 1997; Henquin et al., 2009; Merrins et al., 2010) thereafter. In recent studies, an existence of a different type of Ca^{2+}-dependent K^+ channel, I_{Kslow}, has been reported (Göpel et al., 1999a; Goforth et al., 2002; Zhang et al., 2005).

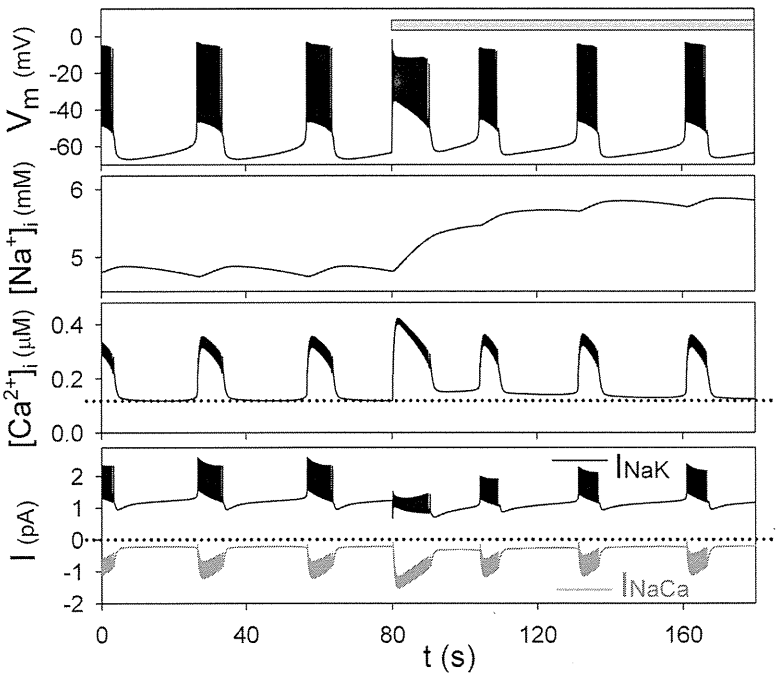

Figure 7. Effects of the inhibition of Na^+/K^+ ATPase by glucose. The inhibition of NaK by glucose was introduced from 80 s (gray bar) by changing F_{glu} (Eq. S55) from 1 to 0.552 at 8 mM [G]. The panels show time courses of V_m, $[Na^+]_i$, $[Ca^{2+}]_i$, I_{NaK}, and I_{NaCa}. Dotted lines indicate the initial basal level of $[Ca^{2+}]_i$ (third panel) and zero current levels (bottom panel).

The important role of I_{Kslow} in terminating the burst via $[Ca^{2+}]$ accumulation was suggested by two mathematical models (Goforth et al., 2002; Fridlyand et al., 2009). To simulate the expected slow kinetics of I_{Kslow}, Goforth et al. (2002) assumed a localized subspace with a substantial volume (occupying ~30% of the cytosolic volume), in which the Ca^{2+} concentration activating I_{Kslow} varies in parallel to changes in $[Ca^{2+}]_{ER}$, rather than the more rapid variation of $[Ca^{2+}]_i$. However, such kinetic changes in I_{Kslow} during the bursting activity nor any histological evidence to justify the diffusion barrier have been found experimentally. Alternatively, Fridlyand et al. (2010) assumed I_{KCas} with an extremely slow time constant of 2.3 s for activation to represent I_{Kslow}. However, SK channels, one of the candidates contributing to the experimental I_{Kslow}, show very fast gating kinetics (Hirschberg et al., 1998).

The slow decay phase of $[Ca^{2+}]_i$ after the burst might lead to slow changes in membrane conductances of several Ca^{2+}-activated channels or transporters. Indeed, the present study suggests that $[Ca^{2+}]_i$ might play a significant role in driving slow interburst depolarization through I_{PMCA}, I_{NaCa}, and I_{TRPM}, as well as $I_{KCa(SK)}$ (Fig. 5). Unfortunately, only a few indirect measurements of these currents have been reported experimentally. As a result, the contribution of I_{TRPM} was only considered in our model, and I_{NaCa} and I_{PMCA} were implemented in a few previous models (Fridlyand et al., 2003; Diederichs, 2006; Meyer-Hermann, 2007).

$[Ca^{2+}]_{ER}$ and I_{SOC}. Repetitive empting and refilling of ER is closely related to bursting rhythm by modulating Ca^{2+}-activated currents. Among them, a store-operated inward current, I_{SOC} (sometimes termed I_{CRAC} or I_{CRAN}), would be a primary candidate to generate the bursting rhythm. Gilon et al. (1999) suggested that ER fills with Ca^{2+} during the burst, and the gradual deactivation of I_{SOC} may lead to termination of the burst. Conversely, the subsequent emptying of the ER after the burst might then reactivate I_{SOC} to trigger a new burst. This mechanism has been tested in several models (Bertram et al., 1995a; Chay, 1996, 1997; Mears et al., 1997; Fridlyand et al., 2003). However, the half-activation concentration of $[Ca^{2+}]_{ER}$ ($K_{0.5,ER}$) has not been measured experimentally, and thus the predicted contributions of I_{SOC} are different among studies. For example, in the models of Chay (1996, 1997) using a $K_{0.5,ER}$ of 50 or 70 µM, the gating of I_{SOC} took a central role in determining the burst rhythm. On the other hand, in the other models I_{SOC} contributed little because the channel remained closed as a result of the assumption of a relatively low $K_{0.5,ER}$ (3 µM; Bertram et al., 1995a, and the present model), or was always open because of an assumed high $K_{0.5,ER}$ (200 µM; Fridlyand et al., 2003). Therefore, it is important for $K_{0.5,ER}$ to be determined experimentally to decide the role of I_{SOC} in generating glucose-induced bursting rhythm under normal conditions. Interestingly, rather consistent effects (the prolongation of the spike burst or the acceleration of the bursting rhythm) were reconstructed with these differing models when I_{SOC} was maximally activated by ER depletion under thapsigargin, muscarinic antagonist, or low glucose (Bertram et al., 1995a; Mears et al., 1997; Fridlyand et al., 2003; the present model).

[ATP] and [ADP] and I_{KATP}. [ATP] and/or [ADP] have been considered as key slow factors, and several β-cell models examined the time-dependent gating of K_{ATP} channels. However, quantitative estimation of the contribution of I_{KATP} to burst activity is highly dependent on the formulation of both I_{KATP} and the metabolic components of each model. For example, Magnus and Keizer (1998) developed a detailed I_{KATP} model and concluded it was a major factor, whereas simulations using the FP model and the same I_{KATP} formulation concluded that I_{KATP} was not of major significance. This is because the two models adopted radically different schemes describing the production of [ATP] and [MgADP].

In addition, it should be noted that ATP-consuming transporters, such as PMCA, SERCA, and NaK, should influence the bursting rhythm by modulating their activities according to the intracellular energy level. However, few studies have dealt with this subject, except the present model by incorporating the detailed kinetic model of I_{NaK} with ΔG_{ATP} dependency.

$[Na^+]_i$ and I_{NaK}. As demonstrated here and in previous modeling studies (Miwa and Imai, 1999; Fridlyand et al., 2003; Meyer-Hermann, 2007), glucose-induced fluctuations of I_{CaV} results in rhythmical Na^+ entry through the action of NCX. Increased $[Na^+]_i$ will activate I_{NaK} and lead to termination of the burst; in turn, a slow decay of $[Na^+]_i$ leads to a decrease in I_{NaK} during the interburst period. Experimentally, Grapengiesser (1996, 1998) observed distinct oscillations of $[Na^+]_i$ under a partial suppression of NaK in mouse β cells. In support of this idea, these oscillations disappeared after inhibition of I_{CaV} or under a lower glucose, but they were insensitive to a blocker of V-dependent Na^+ channels.

$[Na^+]_i$ also modulates the turnover rate of the NCX exchanger. Thus, a proper Na^+ dependency of I_{NaCa} is essential for examination of the role of $[Na^+]_i$ in generating bursting activity. The kinetic scheme of I_{NaCa} used in this study was developed in cardiac cells and has been well tested experimentally. In addition, the tetrodotoxin-sensitive Na^+ current (I_{Na}) might also contribute to intracellular Na^+ accumulation. In preliminary studies, we implemented I_{Na} based on recordings in pancreatic β cells from rat (Hiriart and Matteson, 1988), mouse (Göpel et al., 1999b; Vignali et al., 2006), and human (Braun et al., 2008). However, because I_{Na} was almost completely inactivated at the physiological V_m, the

generated flux was trivial. V_L analysis also revealed that I_{Na} made a very minor contribution to the slow depolarization. Thus, I_{Na} was deleted from the present model.

The $[Na^+]_i$ of 10–14 mM recorded by Grapengiesser (1996) is much higher than the 5.5–7.5 mM in our simulations. When examined with our model, however, 10–14 mM $[Na^+]_i$ resulted in the reverse mode of the NCX all through the normal burst activity because the Na^+-driving force is much reduced. Furthermore, the amplitude of the oscillation of $[Na^+]_i$ and the corresponding effect on I_{NaK} were reliably estimated in our study. This is because the average Na^+ influx through the NCX was determined by the amplitude of I_{CaV} and the action potential frequency, both of which were consistent with experimental data.

Is a single β cell capable of generating full-sized action potentials?

Remarkably, the action potential parameters in our model are quite comparable to experimental measurements in isolated mouse β cells obtained by Smith et al. (1990a) (see Slow fluctuations in [ATP]... in Results). In most papers, however, the amplitude of action potentials was smaller and the quiescent potential less negative when recorded in single β-cell preparations (Rorsman and Trube, 1986; Santos et al., 1991; Kinard et al., 1999; Bertram et al., 2000). It is conceivable that the action potentials might be damped under the patch-clamp recording because the current leak through the gigaseal (~10 GΩ) between the patch electrode and the cell membrane is comparable to the whole cell membrane current (input resistance of ~10–30 GΩ). The membrane capacitance of ~6 pF of small β cells is also in the same order as the floating capacitance of the electrode tip. Moreover, recovery from dissociation injury might be incomplete in culture medium, or action potential generation might be depressed at room temperature or by the rundown of I_{CaV}. It should be noted that mouse or human β cells contain a relatively high density of I_{CaV} ranging over 6 to 11.4 pA pF^{-1}, with an apparent reversal potential of ~50 mV at physiological $[Ca^{2+}]_o$ (see Table I for references). The current densities of I_{CaV} guarantee a fast rising phase and a full size of the action potential in an intact cell before patch-clamp recording. In the present model, the action potential peak was shifted to positive potentials when the membrane K^+ conductance was partially blocked, in agreement with experiments (Atwater et al., 1979; Santos and Rojas, 1989; Rorsman et al., 1992; Houamed et al., 2010). In addition to the action potential amplitude, it should also be noted that the burst duration in single-cell preparations might be affected by the leak conductance and floating capacitance during patch recordings. The difference between electrical activities in single cells and those of islets might be caused by the above recording artifacts.

Further considerations and limitations of the study

The V_L diagram in Fig. 5 indicated prominently large contributions of I_{CaV} during the whole interburst period at both 8 and 16 mM [G]. These contributions are mainly attributable to the increase or decrease in d_{CaV}, which is a pure voltage-dependent gate of I_{CaV}. From the viewpoint that burst–interburst rhythm is principally generated by slow changes in cytosolic substrate concentrations, the role of d_{CaV} is to magnify changes in V_m in the same direction as those induced by other membrane currents under the influence of cytosolic factors. Namely, at 8 mM [G], the slow depolarization induced by changes in I_{KATP} and I_{NaCa} increases d_{CaV}, which results in further depolarization. In the early half of the interburst period at 16 mM [G], d_{CaV} is decreased as a result of the negative shift of V_m, which is primarily induced by a decrease in I_{NaCa} or I_{TRPM} via the progressive decay of $[Ca^{2+}]_i$. During the late phase, the gradual positive shift in V_m induced by a decrease in I_{PMCA} or I_{NaK} increases d_{CaV} to enhance the depolarization. If these secondary contributions of I_{CaV} are excluded from comparison of the membrane currents, the V_L diagram indicates that I_{KATP} and I_{NaCa} at 8 mM [G], and I_{NaCa}, I_{PMCA}, I_{TRPM}, and I_{NaK} at 16 mM [G], play major roles in converting variations in the slow cytosolic factors into the V_m change in our model.

The effects of thapsigargin on $[Ca^{2+}]_i$ have been examined in several experiments using islet preparations, because blocking the ER might provide important clues as to the role of Ca^{2+} buffering by the ER in the bursting rhythm. Unfortunately, there have been no experimental data showing the effects of thapsigargin on the electrical activity or on Ca^{2+} fluctuations in isolated individual β cells. In our single-cell model, the simulation of applying thapsigarin (Fig. 3) was consistent with the accelerated rhythm of the Ca^{2+} fluctuations recorded in several experimental observations in pancreatic islets (Miura et al., 1997; Gilon et al., 1999; Fridlyand et al., 2003), provided that the rhythm of Ca^{2+} transient reflects the electrical

TABLE I

Measurements of the peak of I_{CaV}

Amplitude of I_{CaV}	External solution (mM Ca^{2+})	Species	Reference
51 pA (8.28 pA pF^{-1a})	2.6	mouse	Rorsman et al., 1992
37 pA (6.00 pA pF^{-1a})	2.6	mouse	Islam et al., 1995
70 pA (11.37 pA pF^{-1a})	2.6	mouse	Vignali et al., 2006
93 pA	2.6	mouse	Göpel et al., 1999b
135 pA (21.92 pA pF^{-1a})	10	mouse	Gilon et al., 1997
16 pA pF^{-1}	10	mouse	Arkhammar et al., 1994
16 pA pF^{-1}	10	mouse	Ämmälä et al., 1992
17 pA pF^{-1}	10.2	mouse	Bokvist et al., 1991
6.5 pA pF^{-1}	5	human	Kelly et al., 1991
7 pA pF^{-1}	2.6	human	Braun et al., 2008

[a]Current density.